CHAPTER THREE

# Cascading of Multiscreen Frequency Selective Surfaces

**JOSEPH D. VACCHIONE,** Jet Propulsion Laboratory, California Institute of Technology, Pasadena, California

**RAJ MITTRA,** Electromagnetics Communication Laboratory, University of Illinois at Champaign-Urbana, Urbana, Illinois

Over the past few decades, frequency selective surfaces (FSS) have found numerous applications in both the commercial and military sectors. In addition, for a variety of uses of these structures, the requirements placed on their design specifications have become very stringent. It has been found that a system of two or more layered FSSs are often needed to provide the necessary design degrees of freedom and enable the engineer to meet the stiff design requirements.

The analysis of multiscreen FSS can be divided into two general categories, namely "exact" methods and the approximate "scattering matrix" or "circuit analysis" techniques. Exact methods typically use full-wave moment method techniques [1–6] to determine the unknown current distributions on the FSS screens. The number of unknowns needed to represent these currents depends strongly on the geometry of the elements of the periodic screen comprising the FSS. If $N_1, N_2, \ldots, N_n$ are the number of unknowns on screen 1, screen 2, . . . , and screen $n$, then the moment method solution will involve inverting a matrix with $(N_1 + N_2 + \cdots + N_n)^2$ elements. This matrix size could be a limiting factor that precludes the use of the exact method, particularly when using complex FSS screen geometries requiring many unknowns. To circumvent this difficulty, we could use an iterative

*Frequency Selective Surface and Grid Array*, Edited by T. K. Wu
ISBN 0-471-31189-8 

approach, such as the conjugate gradient method, to solve the problem. This approach, however, could lead to exceedingly large computer run times, which could translate into high cost or even make the analysis impractical.

One way to overcome these difficulties is to employ the scattering matrix technique, which enables the user to represent the solution to an FSS analysis in terms of the generalized scattering parameters [3,7]. It will be shown that this method can obviate the difficulties associated with full-wave techniques without compromising the accuracy needed for most engineering applications. Another advantage associated with this method is that it enables one to analyze multilayered FSS systems comprising screens of vastly dissimilar geometries that would be very difficult to handle with full-wave techniques.

Our goal is to provide the reader with some guidelines for implementing the scattering matrix approach and to introduce a simple procedure for extending the applicability of this methodology to a somewhat larger class of multilayered structures.

In this chapter a time-varying function, $f(t, z)$ is assumed to be time harmonic and is represented by

$$f(z,t) = \mathrm{Re}\{A(z)e^{j\omega t}\}, \tag{3.1}$$

where $A(z)$ is, in general, complex and Re indicates that the real part of the enclosed function should be taken.

## 3.1 REVIEW OF THE SCATTERING MATRIX APPROACH

### 3.1.1 The Scattering Parameters

***Introduction*** In microwave circuit theory, a typical two-port system is represented schematically as in Figure 3.1. In this figure, the incident and reflected fields are represented by the incoming and outgoing waves, $(a_1, a_2)$ and

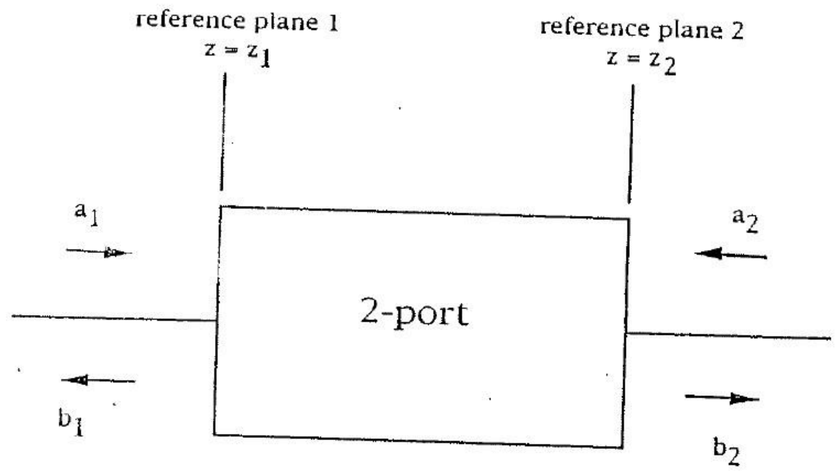


FIGURE 3.1 Schematic representation of a two-port microwave circuit or network.



$(b_1, b_2)$, respectively. The complex amplitudes of the incoming and outgoing waves are defined in terms of the voltage and currents at the respective reference planes as follows:

$$\mathbf{a}_{(1,2)} = \frac{V(z_{(1,2)}, t)}{2\sqrt{Z_0}} + Z_0\frac{I(z_{(1,2)}, t)}{2\sqrt{Z_0}},$$

$$\mathbf{b}_{(1,2)} = \frac{V(z_{(1,2)}, t)}{2\sqrt{Z_0}} - Z_0\frac{I(z_{(1,2)}, t)}{2\sqrt{Z_0}}, \tag{3.2}$$

where $z_{(1,2)}$ defines the reference planes of the two-port as shown in Figure 3.1, $t$ is time, $Z_0$ is the characteristic impedance of the network, $V$ is the voltage evaluated at $z$, and $I$ is the current evaluated at $z$. These waves have the units of $\sqrt{\text{power}}$, and it can be shown that the powers entering and leaving the network are

$$P^{\text{in}} = \tfrac{1}{2}[a_1a_1^* + a_2a_2^*], \qquad P^{\text{out}} = \tfrac{1}{2}[b_1b_1^* + b_2b_2^*]. \tag{3.3}$$

The complex amplitudes at the output and input ports can be related by using a set of constants known as scattering parameters ($S$-parameters):

$$b_1 = a_1S_{11} + a_2S_{12},$$
$$b_2 = a_1S_{21} + a_2S_{22}. \tag{3.4}$$

These equations can be summarized in matrix form as $\mathbf{b} = S\mathbf{a}$, where

$$\mathbf{a} = \begin{bmatrix} a_1 \\ a_2 \end{bmatrix}, \qquad \mathbf{b} = \begin{bmatrix} b_1 \\ b_2 \end{bmatrix}, \qquad S = \begin{bmatrix} S_{11} & S_{12} \\ S_{21} & S_{22} \end{bmatrix}.$$

The expressions for the $S$-parameters can be determined by a linear systems approach. First, suppose the right-side incoming amplitude is set to zero; in other words, we let $a_2 = 0$. Then it follows that

$$S_{11} = \frac{b_1}{a_1} \quad \text{and} \quad S_{21} = \frac{b_2}{a_1}. \tag{3.5}$$

Similarly, if $a_1 = 0$, then

$$S_{12} = \frac{b_1}{a_2} \quad \text{and} \quad S_{22} = \frac{b_2}{a_2}. \tag{3.6}$$

When generalized to the $n$-port case, the scattering matrix $S$ becomes an $n \times n$ matrix and the vectors $\mathbf{a}$ and $\mathbf{b}$ contain $n$ elements each.

In the analysis of an FSS, the scattering matrix representation can be generalized to incorporate the properties of the incident and scattered electromagnetic fields of interest.

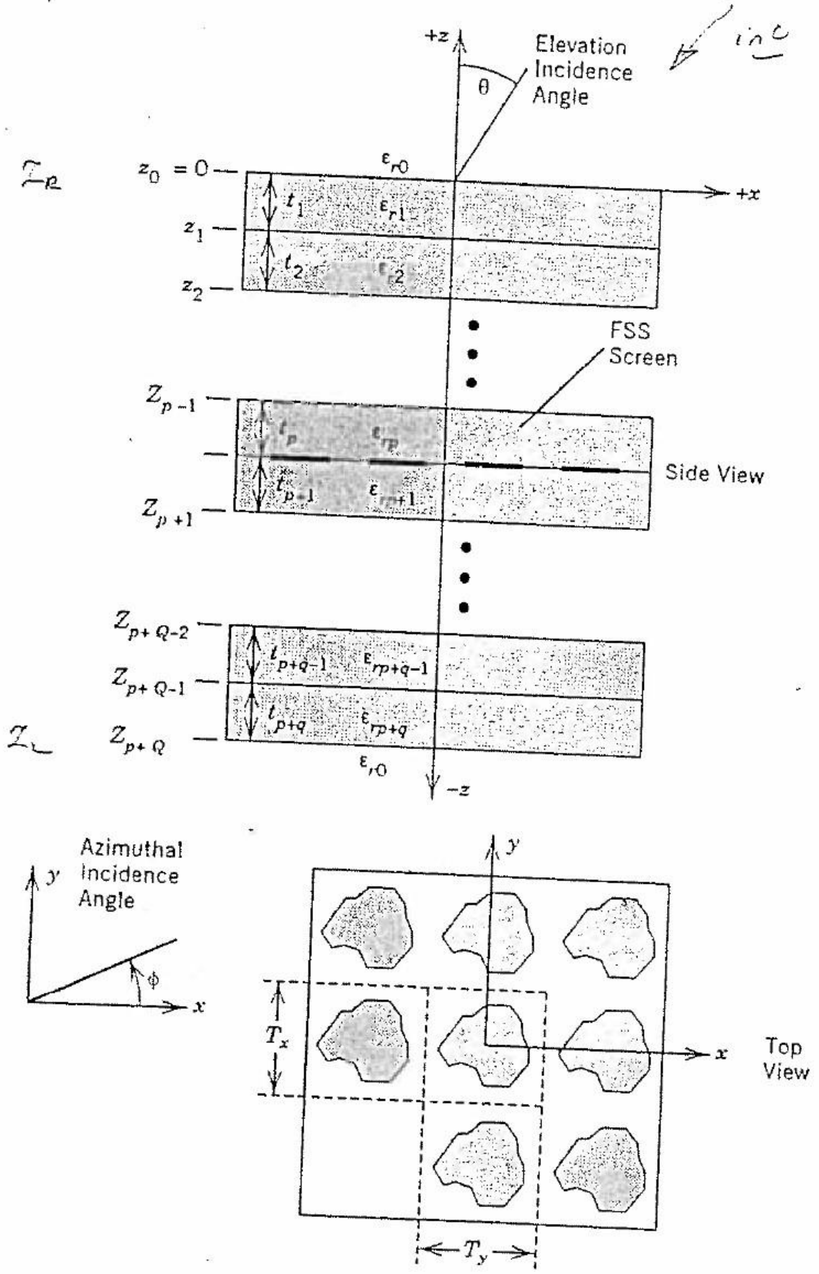


FIGURE 3.2 Infinite, planar, periodic, single-screen FSS geometry.

***Scattering Parameters for a Single-Screen FSS*** By using the spectral-domain approach for analyzing the plane-wave response of the single-screen FSS structure, which is assumed to be infinitesimally thin (Figure 3.2) we can determine the electromagnetic fields at any plane $z = z_n$. These electric fields are expressed in terms of a discrete spectrum of plane waves known as the Floquet harmonics. The $n$th Floquet harmonic corresponds to the $n$th



port in an $n$-port system for which a set of scattering parameters can be defined. Interpreting Eqs. (3.5) and (3.6) in the FSS framework, we see that the $S$-parameters will be the square roots of the ratios of FSS scattered to incident powers. Cwik [3, 7] has defined a set of generalized scattering parameters which incorporate the vector nature of the electromagnetic fields as follows:

$$S^{TE}_{11TE}(m,n;i,j) = \frac{V^{(+,-)}_{TE}(k_{xm},k_{yn},k_{xi},k_{yj},z_L)}{\sqrt{P^{inc}_{TE}(i,j)}},$$

$$S^{TE}_{11TM}(m,n;i,j) = \frac{V^{(+,-)}_{TE}(k_{xm},k_{yn},k_{xi},k_{yj},z_L)}{\sqrt{P^{inc}_{TM}(i,j)}},$$

$$S^{TM}_{11TE}(m,n;i,j) = \frac{V^{(+,-)}_{TM}(k_{xm},k_{yn},k_{xi},k_{yj},z_L)}{\sqrt{P^{inc}_{TE}(i,j)}},$$

$$S^{TM}_{11TM}(m,n;i,j) = \frac{V^{(+,-)}_{TM}(k_{xm},k_{yn},k_{xi},k_{yj},z_L)}{\sqrt{P^{inc}_{TM}(i,j)}},$$

$$S^{TE}_{12TE}(m,n;i,j) = \frac{V^{(-,-)}_{TE}(k_{xm},k_{yn},k_{xi},k_{yj},z_R)}{\sqrt{P^{inc}_{TE}(i,j)}},$$

$$S^{TE}_{12TM}(m,n;i,j) = \frac{V^{(-,-)}_{TE}(k_{xm},k_{yn},k_{xi},k_{yj},z_R)}{\sqrt{P^{inc}_{TM}(i,j)}},$$

$$S^{TM}_{12TE}(m,n;i,j) = \frac{V^{(-,-)}_{TM}(k_{xm},k_{yn},k_{xi},k_{yj},z_R)}{\sqrt{P^{inc}_{TE}(i,j)}},$$

$$S^{TM}_{12TM}(m,n;i,j) = \frac{V^{(-,-)}_{TM}(k_{xm},k_{yn},k_{xi},k_{yj},z_R)}{\sqrt{P^{inc}_{TM}(i,j)}},$$

$$S^{TE}_{21TE}(m,n;i,j) = \frac{V^{(+,+)}_{TE}(k_{xm},k_{yn},k_{xi},k_{yj},z_L)}{\sqrt{P^{inc}_{TE}(i,j)}},$$

$$S^{TE}_{21TM}(m,n;i,j) = \frac{V^{(+,+)}_{TE}(k_{xm},k_{yn},k_{xi},k_{yj},z_L)}{\sqrt{P^{inc}_{TM}(i,j)}},$$

$$S_{21\mathrm{TE}}^{\mathrm{TM}}(m,n;i,j) = \frac{V_{\mathrm{TM}}^{(+,+)}(k_{xm},k_{yn},k_{xi},k_{yj},z_L)}{\sqrt{P_{\mathrm{TE}}^{\mathrm{inc}}(i,j)}},$$

$$S_{21\mathrm{TM}}^{\mathrm{TM}}(m,n;i,j) = \frac{V_{\mathrm{TM}}^{(+,+)}(k_{xm},k_{yn},k_{xi},k_{yj},z_L)}{\sqrt{P_{\mathrm{TM}}^{\mathrm{inc}}(i,j)}},$$

$$S_{22\mathrm{TE}}^{\mathrm{TE}}(m,n;i,j) = \frac{V_{\mathrm{TE}}^{(-,+)}(k_{xm},k_{yn},k_{xi},k_{yj},z_R)}{\sqrt{P_{\mathrm{TE}}^{\mathrm{inc}}(i,j)}},$$

$$S_{22\mathrm{TM}}^{\mathrm{TE}}(m,n;i,j) = \frac{V_{\mathrm{TE}}^{(-,+)}(k_{xm},k_{yn},k_{xi},k_{yj},z_R)}{\sqrt{P_{\mathrm{TM}}^{\mathrm{inc}}(i,j)}},$$

$$S_{22\mathrm{TE}}^{\mathrm{TM}}(m,n;i,j) = \frac{V_{\mathrm{TM}}^{(-,+)}(k_{xm},k_{yn},k_{xi},k_{yj},z_R)}{\sqrt{P_{\mathrm{TE}}^{\mathrm{inc}}(i,j)}},$$

$$S_{22\mathrm{TM}}^{\mathrm{TM}}(m,n;i,j) = \frac{V_{\mathrm{TM}}^{(-,+)}(k_{xm},k_{yn},k_{xi},k_{yj},z_R)}{\sqrt{P_{\mathrm{TM}}^{\mathrm{inc}}(i,j)}}, \qquad (3.7)$$

where

$z_R$ = rightmost interface in Figure 3.2 = 0,

$z_L$ = leftmost interface in Figure 3.2 = $z_{P+Q}$,

and

$$V_{\mathrm{TE}}^{(\pm,\pm)}(k_{xm},k_{yn},k_{xi},k_{yj},z) = \bar{f}(m,n,i,j,z)^{(\pm,\pm)}\sqrt{P_{\mathrm{TE}}(m,n)},$$

$$V_{\mathrm{TM}}^{(\pm,\pm)}(k_{xm},k_{yn},k_{xi},k_{yj},z) = \bar{a}(m,n,i,j,z)^{(\pm,\pm)}\sqrt{P_{\mathrm{TM}}(m,n)}$$

are Cwik's normalized Floquet voltage waves. Referring to the coordinate system of Figure 3.2, we see that the $(\pm,\pm)$ notation associated with the definition for the voltage waves indicates the direction, either $+z$ or $-z$, of the incident and scattered energy in the FSS system. The first element of the pair corresponds to the scattered waves, and the second element of the pair corresponds to the incident waves—that is, (scattered, incident). Thus, the Floquet voltage wave, $V^{(+,-)}(m,n;i,j)$, contains information about the $(m,n)$th harmonic reflected (into the $+z$ direction) from the leftmost reference plane due to the $(i,j)$th plane wave incident (from the $-z$ direction) on this plane. Similarly, $V^{(-,-)}(m,n;i,j)$ contains information about the $(m,n)$th harmonic transmitted through the FSS structure due to the $(i,j)$th plane wave incident on the leftmost reference plane. Finally, $V^{(+,+)}(m,n;i,j)$ and $V^{(-,+)}(m,n;i,j)$ contain information about the $(m,n)$th transmitted and reflected harmonics, respectively, due to the $(i,j)$th plane wave incident on



the rightmost reference plane. The voltage waves are defined in terms of the transforms of the electric and magnetic vector potentials, $\bar{f}(m,n,z)$ and $\bar{a}(m,n,z)$, respectively. For computing the scattering parameters, these vectors potentials are evaluated at the leftmost and rightmost reference planes of the FSS. In that situation the vector potentials can be written as

$$\bar{f}(m,n,i,j,z)^{(\pm,\pm)} = \bar{F}(m,n,i,j)^{(\pm,\pm)}e^{\gamma_{mn}z},$$

$$\bar{a}(m,n,i,j,z)^{(\pm,\pm)} = \bar{A}(m,n,i,j)^{(\pm,\pm)}e^{\gamma_{mn}z}. \qquad (3.8)$$

The propagation constant, $\gamma_{mn}$, is defined by

$$\gamma_{mn}(z) = \begin{cases} -\sqrt{k_{xm}^2 + k_{yn}^2 - k_0^2} & \text{for } z > z_L, \\ +\sqrt{k_{xm}^2 + k_{yn}^2 - k_0^2} & \text{for } z < z_R, \end{cases} \qquad (3.9)$$

where the sign of the radical was chosen to satisfy the radiation condition.

In the past, the leftmost and rightmost reference planes were chosen to coincide with the plane containing the FSS screen. If a screen supported by a dielectric substrate and/or superstrate was being considered, the scattering parameters of each dielectric layer and the FSS screen would be computed individually and the entire system would be cascaded by using the scattering matrix approach, as depicted in Figure 3.3(a). It has been found, however, that this approach can lead to erroneous results for reasons that will be discussed shortly. The appropriate method for handling this situation is to define the reference planes at the outer dielectric layer as shown in Figure 3.3(b). This approach requires that the analysis procedure used to study the single-screen system be capable of incorporating the dielectric superstrates and substrates by defining the scattering matrix of the composite system.

The normalization factors employed in Equation (3.7) are the square roots of power in the $(m,n)$th Floquet harmonic with TE (electric field transverse to the $z$-direction) or TM (magnetic field transverse to the $z$-direction) polarization. These factors are

$$P_{\mathrm{TE}}(m,n) = \left(k_{xm}^2 + k_{yn}^2\right)Y_{mn}^{\mathrm{TE}}, \qquad P_{\mathrm{TM}}(m,n) = \frac{k_{xm}^2 + k_{yn}^2}{Y_{mn}^{\mathrm{TM}}}, \qquad (3.10)$$

where

$$Y^{\mathrm{TM}} = \frac{j\omega\epsilon}{\gamma_{mn}}, \qquad Y^{\mathrm{TE}} = \frac{\gamma_{mn}}{j\omega\mu}$$

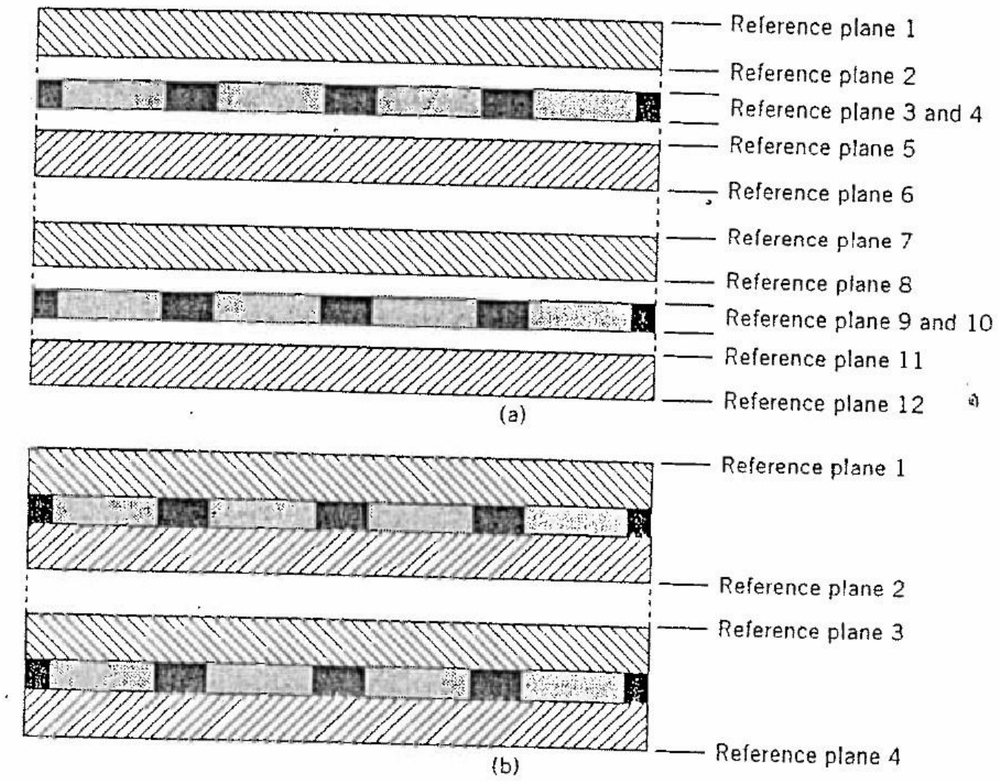


FIGURE 3.3 Two methods for subdividing a multilayered FSS system. (a) A reference plane can be positioned at each interface in the system; this method leads to the requirement of an inordinately large number of harmonics in the scattering matrix of the FSS screen portions between reference planes 3 and 4 and reference planes 9 and 10. (b) The requirement that every FSS screen be surrounded by at least one dielectric substrate and superstrate leads to scattering matrices that are manageable.

The terms $k_{xm}$ and $k_{yn}$ are the wave numbers of the Floquet space harmonics that determine the nature of the scattered electromagnetic field spectrum. They are defined as

$$k_{xm} = \frac{2\pi}{T_x} m + k_x^{\text{inc}}, \qquad k_{yn} = \frac{2\pi}{T_y} n + k_y^{\text{inc}}, \tag{3.11}$$

where $k_x^{\text{inc}} = k_0 \sin\theta_{\text{inc}} \cos\phi_{\text{inc}}$ and $k_y^{\text{inc}} = k_0 \sin\theta_{\text{inc}} \sin\phi_{\text{inc}}$. The incident harmonics are functions of the elevation angle, $\theta_{\text{inc}}$, and the azimuthal angle, $\phi_{\text{inc}}$.

When the FSS system is lossless, the Floquet voltage waves exhibit an outward-bound traveling-wave nature for $k_{xm}^2 + k_{yn}^2 < k_0^2$, and an evanescent-wave behavior when $k_{xm}^2 + k_{yn}^2 > k_0^2$. It may be easily verified that only a finite number of the infinite spectrum of Floquet voltage waves correspond to propagating harmonics. From a design standpoint, it is usually desirable to have only a single propagating harmonic, and the higher-order grating lobes



can be suppressed by requiring that the unit-cell dimensions of the periodic screen satisfy the conditions $T_x < \lambda/2$ and $T_y < \lambda/2$. In this way, the zeroth-order harmonic ($m = 0$, $n = 0$) is guaranteed to be the only propagating Floquet voltage wave.

As a final note regarding the scattering parameters of Eq. (3.7), we observe that it is often more convenient to reexpress the transforms of the vector potentials used in the definition of the Floquet voltage waves in terms of the transforms of the electric fields. The electric and magnetic vector potentials, expressed in terms of the total electric fields, are

$$\tilde{f}(m,n,i,j,z)^{(\pm,\pm)} = \frac{j\left(k_{yn}\tilde{E}^{\pm}_{x_{\text{total}}} - k_{xm}\tilde{E}^{\pm}_{y_{\text{total}}}\right)}{k_{xm}^2 + k_{yn}^2},$$

$$\tilde{a}(m,n,i,j,z)^{(\pm,\pm)} = \frac{\omega\epsilon}{\gamma_{mn}} \frac{k_{xm}\tilde{E}^{\pm}_{x_{\text{total}}} + k_{yn}\tilde{E}^{\pm}_{y_{\text{total}}}}{k_{xm}^2 + k_{yn}^2}. \tag{3.12}$$

The $\tilde{E}^{\pm}_{\text{total}}$'s can be found as follows:

$$\tilde{E}^{+}_{(x,y)_{\text{total}}}(k_{xm},k_{yn}) = \tilde{E}^{+}_{(x,y)_s} + E_{(x,y)_{\text{ref}}}\delta(k_{xi}-k_{xm})\delta(k_{yj}-k_{yn}),$$
$$\tilde{E}^{-}_{(x,y)_{\text{total}}}(k_{xm},k_{yn}) = \tilde{E}^{-}_{(x,y)_s} + E_{(x,y)_{\text{trans}}}\delta(k_{xi}-k_{xm})\delta(k_{yj}-k_{yn}), \tag{3.13}$$

where $E_{(\text{ref, trans})}$ are the electric fields, evaluated at $z = 0$ and $z = z_{P+Q}$, which would be reflected and transmitted in the dielectric layers in the absence of the FSS screen. These field components are added to the total fields only when the incident harmonic is equal to the scattered harmonic as indicated by the Kronecker delta, $\delta(k_{xi} - k_{xm})\delta(k_{yj} - k_{yn})$ in (3.13). Finally, $\tilde{E}_s^{(+,-)}$ is the scattered harmonic evaluated at $z = 0$ and $z = z_{P+Q}$.

Using Eq. (3.12), we write the scattering parameters in terms of the electric fields evaluated at the leftmost and rightmost reference planes. This has been carried out for the reflection coefficient $S_{11}$; the other scattering parameters can be written in a similar fashion.

$$S^{\text{TE}}_{11\text{TE}}(m,n,i,j) = \sqrt{\frac{Y^{\text{TE}}_{mn}}{Y^{\text{TE}}_{ij}}} \frac{j\left(k_{yn}\tilde{E}^{+}_{x_{\text{total}}} - k_{xm}\tilde{E}^{+}_{y_{\text{total}}}\right)}{\sqrt{\left(k_{xm}^2 + k_{yn}^2\right)\left(k_{xi}^2 + k_{yj}^2\right)}},$$

$$S^{\text{TE}}_{11\text{TM}}(m,n,i,j) = \sqrt{Y^{\text{TE}}_{mn}Y^{\text{TM}}_{ij}} \frac{j\left(k_{yn}\tilde{E}^{+}_{x_{\text{total}}} - k_{xm}\tilde{E}^{+}_{y_{\text{total}}}\right)}{\sqrt{\left(k_{xm}^2 + k_{yn}^2\right)\left(k_{xi}^2 + k_{yj}^2\right)}},$$

$$S^{\text{TM}}_{11\text{TE}}(m,n,i,j) = \frac{\omega\epsilon}{\gamma_{mn}} \sqrt{\frac{1}{Y^{\text{TM}}_{mn}Y^{\text{TE}}_{ij}}} \frac{k_{xm}\tilde{E}^{+}_{x_{\text{total}}} + k_{yn}\tilde{E}^{+}_{y_{\text{total}}}}{\sqrt{\left(k_{xm}^2 + k_{yn}^2\right)\left(k_{xi}^2 + k_{yj}^2\right)}},$$

$$S^{\text{TM}}_{11\text{TM}}(m,n,i,j) = \frac{\omega\epsilon}{\gamma_{mn}} \sqrt{\frac{Y^{\text{TM}}_{ij}}{Y^{\text{TM}}_{mn}}} \frac{k_{xm}\tilde{E}^{+}_{x_{\text{total}}} + k_{yn}\tilde{E}^{+}_{y_{\text{total}}}}{\sqrt{\left(k_{xm}^2 + k_{yn}^2\right)\left(k_{xi}^2 + k_{yj}^2\right)}}. \tag{3.14}$$

### 3.1.2 The Scattering Matrix

Since a periodic FSS scatters an incident plane wave into a discrete spectrum of Floquet harmonics, it is convenient to represent the scattered fields in modular matrix form. The principle advantage of this form is that it can be used to replace the single-screen FSS by a mathematical representation that can be manipulated at the system level to obtain a composite response of a multiscreen FSS structure. At the interface of two single-screen FSS systems, the harmonics scattered from one structure become the incident fields for the other. This implies that the scattering matrix must contain the scattered field representations due to an entire spectrum of incident field harmonics. Thus, in principle, the matrix is a doubly infinite array, each of whose columns represents the scattered field due to a given incident harmonic. The elements of this matrix are the scattering parameters defined in Section 3.1.1. These elements are organized into four distinct matrices corresponding to the four scattering parameters $S_{11}$, $S_{12}$, $S_{21}$, and $S_{22}$. Each matrix is composed of four polarization quadrants corresponding to the two copolarized components ($S_{TE}^{TE}$ and $S_{TM}^{TM}$) and the two cross-polarized components ($S_{TM}^{TE}$ and $S_{TE}^{TM}$). Each matrix element is associated with a harmonic in the two-dimensional Floquet spectrum and is arranged as shown in Figure 3.4.

One of the more elusive issues regarding the scattering matrix is the determination of the number of harmonics that need to be included to obtain accurate numerical results when manipulating the matrices at the system level. Truncation of the scattering matrix is principally a numerical task facilitated by studying the behavior of the scattering parameters as a function of the harmonic number and the location of the reference planes at which they are evaluated.

After the study of a great number of FSS structures where a single dielectric superstrate and a substrate surround the FSS screen, it has been found that the scattering parameters decay exponentially for increasing $\gamma_{mn}$ (i.e., for increasing order of $m$ and $n$) and $\Delta z$; that is, the $S$-parameters approximately behave as

$$|S_{mn}| \sim e^{-\gamma_{mn}\Delta z} \tag{3.15}$$

In reality, the $S$-parameters have a damped sinusoidal characteristic, but the previous expression represents the envelope of the $S$-parameters' decay. This means that for a given value of $\Delta z$, it is possible to identify a value of $\gamma_{mn} = \gamma_{mn_{max}}$ for which the scattering parameters have decayed to a sufficiently small value as to be considered numerically zero. The scattering parameters associated with the wave numbers for which $\gamma_{mn}$ is larger than $\gamma_{mn_{max}}$ can also be considered to be numerically zero and will therefore not be needed in the matrix representation of the scattered field. It is easy to see that as $\Delta z$ becomes larger, the maximum value of the propagation constant, $\gamma_{mn_{max}}$, becomes smaller, which implies that fewer harmonics are needed to



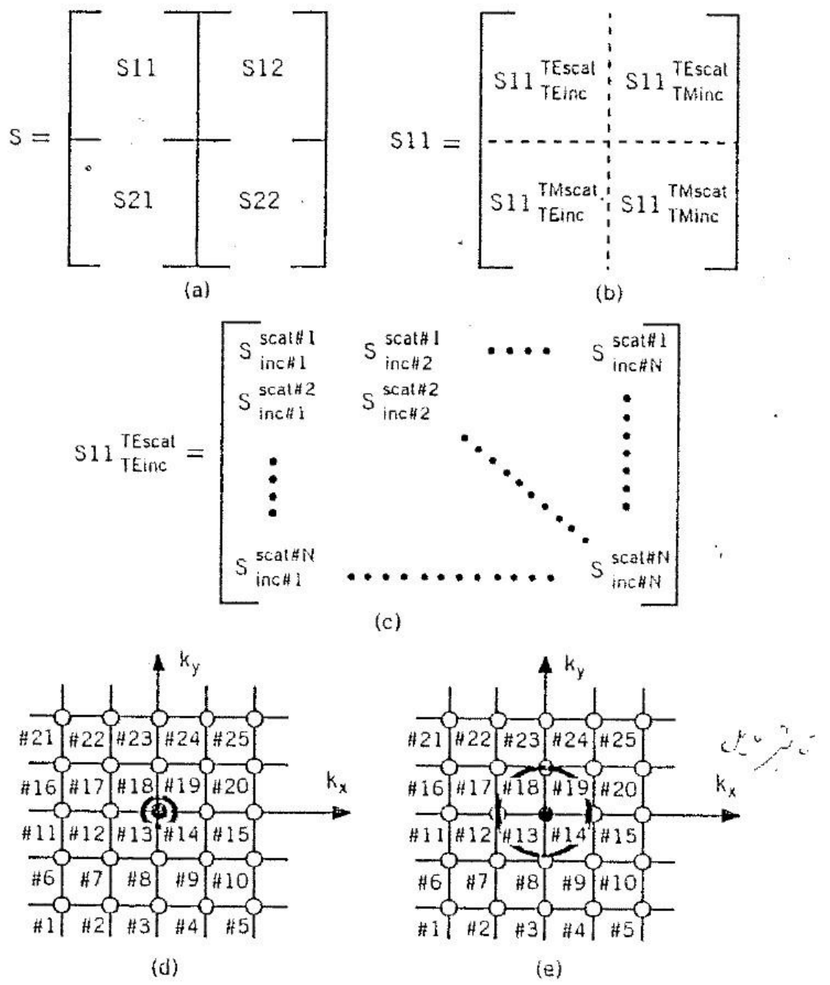


FIGURE 3.4 The scattering matrix. (a) The entire scattering matrix system. (b) The subdivision of S11 into its four polarization quadrants. (c) The ordering of a polarization quadrant. (d) The $k$-space diagram and the correspondence between matrix elements and Floquet harmonics. In this case the FSS is designed to reject grating lobes. (e) The $k$-space diagram for an FSS that will have grating lobes for nonzero angles of incidence.

represent the scattered fields. Conversely, if $\Delta z$ is very small, then $\gamma_{mn_{max}}$ will be large. As mentioned, the reference plane is often chosen to coincide with the plane of the FSS screen ($\Delta z = 0$); in this situation, an inordinately large number of harmonics may be required in the scattering matrix, so it is recommended that a dielectric layer always be included above and below the FSS screen when computing the $S$-matrix parameters.

Having observed that $|S_{mn}|$ approaches zero for increasing harmonic numbers, one may ask: What value of $|S_{mn}|$ is small enough to be considered

"numerically zero"? As an answer to this question, a numerical criterion or rule of thumb has been established. This has been determined by performing numerous numerical experiments in which composite solutions, found by using scattering matrices containing differing numbers of harmonics, were compared with a benchmark. Such a benchmark is readily available for the special subcase where the FSS system is image symmetric; that is, there exists a mirror-image symmetry at the plane containing the FSS screen as shown in Figure 3.5. For this case, an "exact" solution can be found very efficiently as depicted in Figure 3.5. The method, known as the image screen technique, entails the splitting of the dual-screen problem into two, easily solved, single-screen problems.

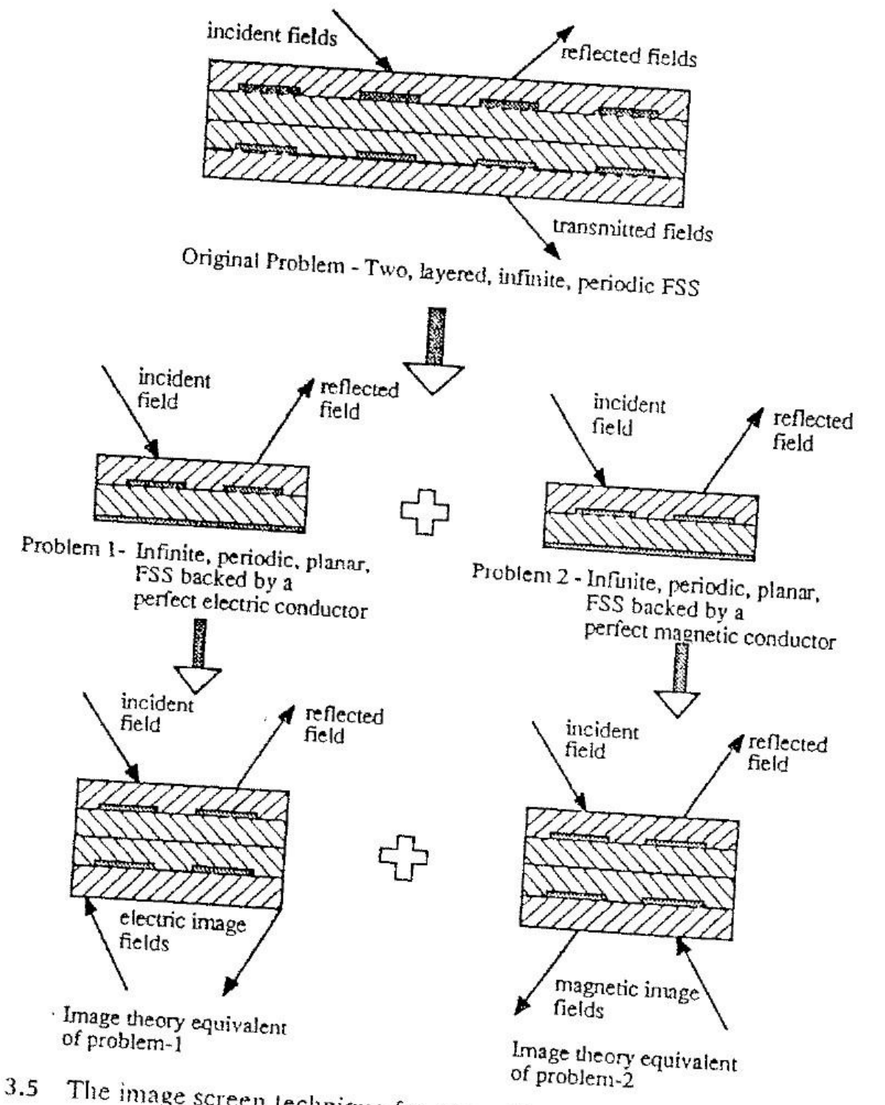


FIGURE 3.5 The image screen technique for computing the currents on a symmetric, dual-screen FSS system.



Some representative results of the numerical experimentation are shown in Figures 3.6 and 3.7 for the simple case of a symmetrical dual-screen strip grating. Note that the strip grating has a one-dimensional Floquet spectrum. In these figures, the frequency responses of the reflection coefficient, computed by using scattering matrices containing 1, 5, and 9 harmonics, are compared to the results derived by the image screen technique. In addition, the magnitudes of the harmonics are plotted as functions of the harmonic number. As can be seen, when the screen separation, $\Delta z$, is 2.0 cm (Figure 3.6), all four methods give equally good results. In other words, in this case, only one harmonic needs to be retained in the scattering matrix. Also note that the magnitudes of all higher-order harmonics are lower than $-22$ dB.

In the second case, where $\Delta z = 0.02$ cm (Figure 3.7), none of the scattering matrix approaches gives the same result as the "exact" approach. Note that the magnitude of the highest-order harmonic shown has a value greater than $-22$ dB. Indeed, it has been found that if the magnitude of the higher-order harmonic has a value of $-22$ dB or larger, then it and all the lower-order harmonics, even if these harmonics have a magnitude less than $-22$ dB, should be included in the scattering matrix. Thus, once the higher-order harmonics have permanently decayed to a value of $-22$ dB or less (i.e., no higher-order harmonic is greater than $-22$ dB), the matrix can be truncated. This is a conservative rule of thumb, since, although it is possible that the scattering matrix that has been truncated before the harmonics have decayed to $-22$ dB will give good results when forming a composite system, it is useful to use the $-22$-dB rule to guarantee that the results are consistently good.

We now point out the significance of the $k$-space diagrams of Figures 3.4(d and e). In this instance, 25 scattered harmonics are included in the scattering matrix. In Figure 3.4(d) the FSS is designed to prevent the appearance of grating lobes. This is indicated by the presence of only one harmonic within the circle defined by $k_{xm}^2 + k_{yn}^2 < k_0^2$. For the case where the fields incident upon this FSS are normal to the plane of FSS (i.e., $\theta = \phi = 0°$), the scattered harmonics with the greatest magnitude will correspond to the harmonic located at the origin of the $k$-space diagram (harmonic number 13 in this case). In the event that the incident energy is not normal to the plane of this FSS, the scattered harmonics will shift to a different location in the $k$-space diagram. Since the FSS is designed to prevent grating lobes, harmonic 13 will either shift to a location within the circle and no other harmonics will enter into the circle or it will shift out of the circle but still no other harmonics will shift into the circle. The latter situation represents the phenomenon of total internal reflection; that is, no propagating harmonics are scattered from the FSS. For Figure 3.4(d), the scattering matrix can be compiled by using the matrix elements indicated in the figure with harmonic 13 being the central element.

If the criterion that guarantees the absence of grating lobes is not adhered to, then more than one harmonic may be present in the circle, as shown in Figure 3.4(e). This situation may arise for all angles of incidence ($-90° <$

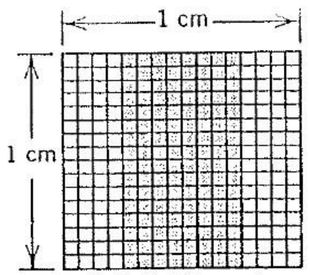


Unit-Cell Geometry
(for both FSS screens)
Strip Grating

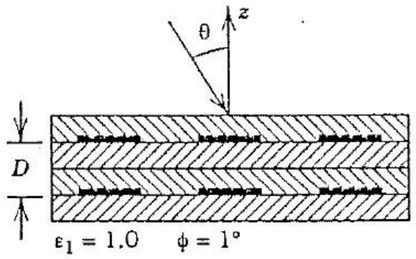


Side View of Dual-Screen FSS

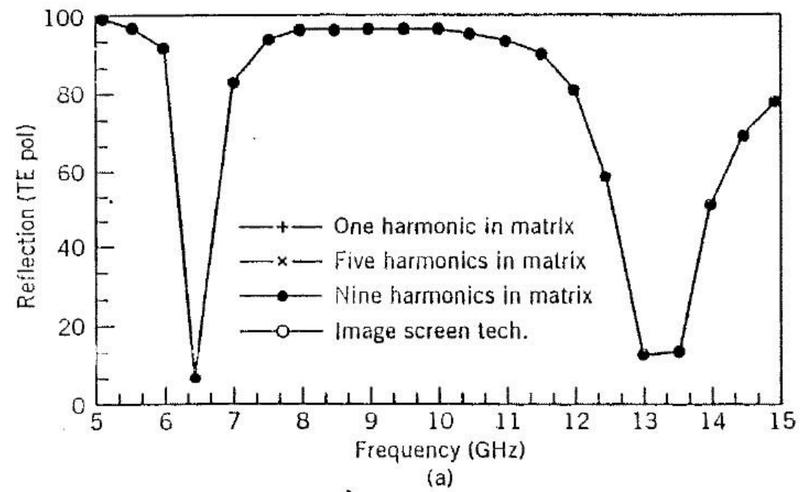


(a)

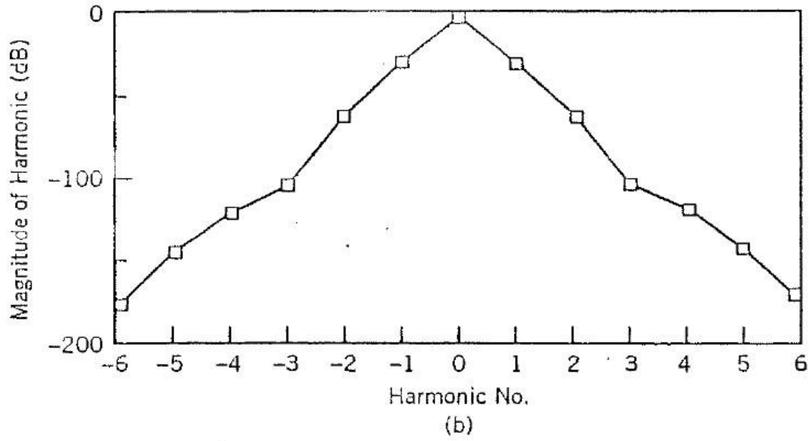


(b)

**FIGURE 3.6** Truncation criterion study. Screen separation, $D = 2$ cm. (a) Comparison of power reflection coefficient vs. frequency computed by cascading scattering matrices with one harmonic, five harmonics, and nine harmonics. These results are then compared to the "exact" values using the image screen technique. (b) Magnitude of the harmonic vs. harmonic number. Note that, when all the harmonics with magnitudes greater than −22 dB are used in the scattering matrices, good results are obtained with the cascading procedure.



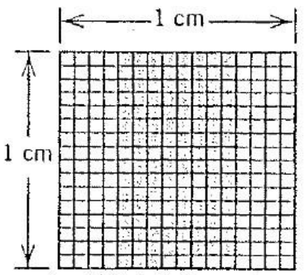


Unit-Cell Geometry
(for both FSS screens)
Strip Grating

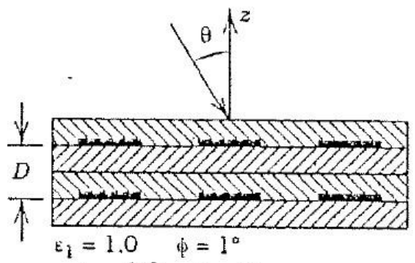


Side View of Duel-Screen FSS

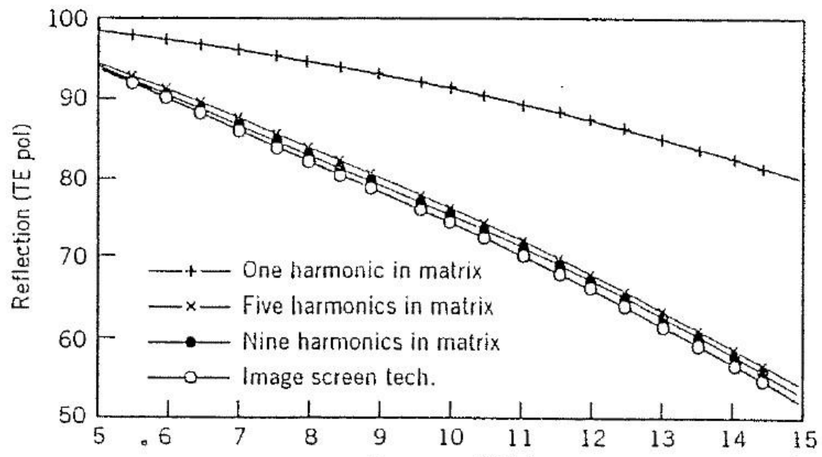


(a)

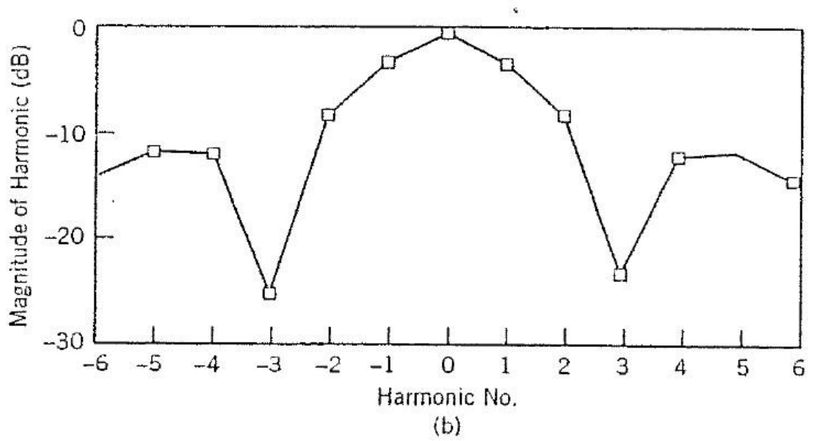


(b)

**FIGURE 3.7** Truncation criterion study. Screen separation, $D = 0.02$ cm. (a) Comparison of power reflection coefficient vs. frequency computed by cascading scattering matrices with one harmonic, five harmonics, and nine harmonics. These results are then compared to the "exact" values using the image screen technique. (b) Magnitude of the harmonic vs. harmonic number. Note that, when all the harmonics with magnitudes greater than −22 dB are used in the scattering matrices, good results are obtained when cascading.

$\theta < 90°$), or it may occur only for special angles of incidence. In Figure 3.4(e), for $\theta = 0°$, no grating lobes are present; however, if $\theta > 0°$, then one of the higher-order harmonics can shift into the circle along with the zeroth-order harmonic, thus producing a grating lobe. If one or more grating lobes appear in the scattered field, it is important to include, as a minimum, all propagating harmonics in the scattering matrix.

In addition to the truncation of the higher-order harmonics, scattering matrix size can be substantially reduced in the special instances when the cross-polarized scattering parameters are very small, about $1 \times 10^{-4}$ or less. When this is the case, the scattering matrix can be split into two systems containing TE or TM copolarized parameters only. In this way, the analysis of a multiscreen system can be carried out separately for each polarization by using scattering matrices that are a factor of 4 times smaller than needed in the full-matrix approach.

## 3.2 CASCADING TECHNIQUES

Once finite-sized scattering matrices for the single-layered FSS systems are computed, a number of analytical procedures are available for obtaining a composite, multilayered, system representation. It is possible to make direct use of the $S$-matrix (scattering matrix) in conjunction with the following matrix equations to obtain a composite system representation for the two-layered single-screen systems:

$$\begin{cases} S_{11}^C = S_{11}^{(1)} + S_{12}^{(1)} R S_{11}^{(2)} S_{21}^{(1)}, \\ S_{12}^C = S_{12}^{(1)} R S_{12}^{(2)}, \\ S_{21}^C = S_{21}^{(2)} T S_{21}^{(1)}, \\ S_{22}^C = S_{22}^{(2)} + S_{21}^{(2)} T S_{22}^{(1)} S_{12}^{(2)}, \end{cases} \tag{3.16}$$

where $\mathbf{R} = [1 - S_{11}^{(2)} S_{22}^{(1)}]^{-1}$ and $\mathbf{T} = [1 - S_{22}^{(1)} S_{11}^{(2)}]^{-1}$, $S_{11}^{(1)}$, $S_{12}^{(1)}$, $S_{21}^{(1)}$, and $S_{22}^{(1)}$ are the scattering matrices representing the first FSS system, and $S_{11}^{(2)}$, $S_{12}^{(2)}$, $S_{21}^{(2)}$, and $S_{22}^{(2)}$ are the scattering matrices associated with the second FSS system. If more than two single-screen subsystems make up the entire multilayered system, then the composite system is formed by repeatedly cascading the additional subsystems to the composite system until all layers have been appended to the multilayered structure.

It is instructive to point out that the cascading approach is a computationally efficient method for studying the properties of a multilayered system. Once the scattering matrix has been computed, the remainder of the effort involves simple matrix addition, multiplication, and inversion. No restrictions are placed on the geometries of the individual planar FSS subsystems, giving the flexibility to easily form a large variety of multilayered structures. The



major limitation of the cascading approach is the number of harmonics that can be stored in the scattering matrix. This number, of course, is a function of the computer used to carry out the analysis.

Care must also be exercised when the periodicities of the individual subsystems of the multilayered structure are different [8]. This situation is depicted in Figure 3.8 for three different one-dimensional two-screen systems. When the multilayered system comprises subsystems of equal periodicity, as in Figure 3.8(a), the same Floquet set is scattered from the individual subsystems as well as the composite multilayered system. The reason for this is easily seen from Eq. (3.11) which determines the nature of the scattered harmonics. The equation shows that the Floquet harmonics explicitly dependent on the periodicities $T_x$ and $T_y$ of the FSS; this implies, in turn, that for the equal-periodicity dual-screen case, a single Floquet set is considered when computing the scattering matrices of the individual subsystems for use in the cascading procedure. This is in contrast to the instances depicted in Figures 3.8(b) and (c), where the subsystems have different periodicities. In this situation the scattering matrices of the individual subsystems can no longer be computed a priori as was possible for the equal-periodicity case. Instead, the multilayered structure must first be specified and a system period found by studying that structure in its entirety. In Figure 3.8(b), the individual subsystem periods are $T_1$ and $T_2$, and the system period is $T_{sys} = T_2$. Similarly, in Figure 3.8(c), the subsystem periods are $T_1$ and $T_2$ and the system period is $T_{sys} = 2T_1 = 3T_2$. In general, given any multilayered structure, it is possible to find an overall system period, although in some cases this period may be quite a bit larger than those of the individual subsystems. Once $T_{sys}$ has been determined, the set of Floquet harmonics that will be scattered from the multilayered structure can be associated with the wave numbers

$$k_{xm} = \frac{2\pi}{T_{\text{Sys}\,x}} m + k_x^{\text{inc}}, \qquad k_{yn} = \frac{2\pi}{T_{\text{Sys}\,y}} n + k_y^{\text{inc}}. \tag{3.17}$$

The scattering matrices of the individual subsystems will subsequently be computed so that their elements correspond to the system Floquet harmonics. Notice that since $T_{sys}$ is greater than or equal to the periodicities of the individual subsystems, the scattered harmonics will be more densely packed; hence, a larger number of harmonics will be needed in the scattering matrices to satisfy the truncation criterion.

In addition to the extra harmonics that need to be included in the scattering matrices of the unequal-periodicity subsystems, special consideration has to be given when computing the scattering parameters. For instance, suppose that $T_2 = 2\pi$ and $\theta = \phi = 0°$ in Figure 3.8(b); then the system Floquet set will be given by $0, \pm 1, \pm 2, \pm 3, \pm 4, \ldots$. In order to compute a

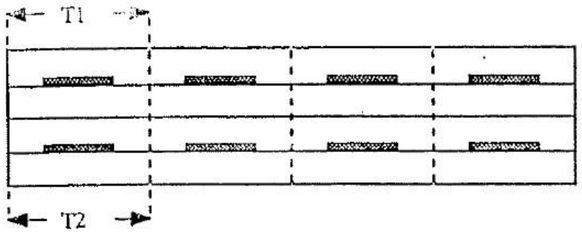


(a)

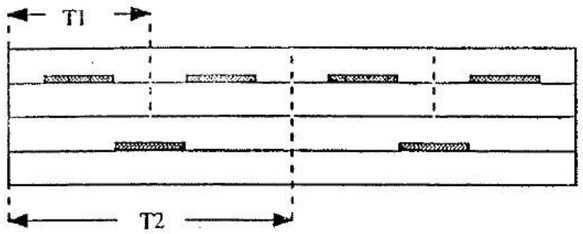


(b)

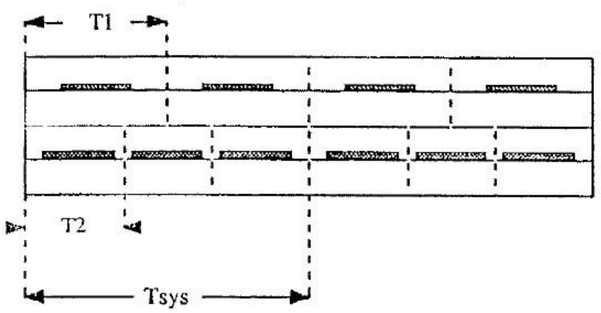


(c)

**FIGURE 3.8** Comparison of the system periods for equal- and unequal-periodicity systems. (a) Equal-periodicity case, $T_1 = T_2 = T_{sys}$. (b) Unequal-periodicity case, 1:2 ratio between the periods of the two screens, $2T_1 = T_2 = T_{sys}$. (c) Unequal-periodicity case, 2:3 ratio between the periods of the two screens, $2T_1 = 3T_2 = T_{sys}$.

scattering matrix, each of the system Floquet harmonics is allowed to illuminate the FSS structure, and the scattered sets due to each of these incident harmonics are used to make up the columns of the matrix. Now, when the scattering parameters due to the zeroth-order Floquet harmonic for the top subsystem are computed, the scattered harmonics appear at $0, \pm 2, \pm 4, \ldots$. In order to fill the scattering matrix for the top subsystem as prescribed by the system Floquet set, zeros must be placed at the matrix locations corresponding to the $\pm 1, \pm 3, \ldots$ Floquet harmonics. Similarly, when the $+1$ Floquet harmonic is incident, the harmonics scattered from the top subsys-



tem appear at $\pm 1, \pm 3, \ldots$, so zeros must be placed at the locations corresponding to the $0, \pm 2, \pm 4, \ldots$, Floquet harmonics. Thus, for the top subsystem of Figure 3.8(b), the scattering matrix has every other element set to zero as we show here for a system of four nonzero harmonics. Note that this corresponds to a one-dimensional FSS where only the $k_x$ Floquet harmonics are considered and for which no cross-polarization is considered. The columns of the matrix are therefore composed of the $n$ scattered $k_x$ harmonics as shown in Eq. (3.18):

$$\mathbf{S}_{11}^{1} = \begin{bmatrix} S_{11}(1) & 0 & S_{11}(3) & 0 \\ 0 & S_{11}(6) & 0 & S_{11}(8) \\ S_{11}(9) & 0 & S_{11}(11) & 0 \\ 0 & S_{11}(14) & 0 & S_{11}(16) \end{bmatrix}. \tag{3.18}$$

Since the periodicity of the bottom subsystem is equal to $T_{sys}$, it would scatter all the system harmonics so that its scattering matrix would be "full." In a similar way, the form of the scattering matrices for the system in Figure 3.8(c) is

$$\mathbf{S}_{11}^{1} = \begin{bmatrix} S_{11}(1) & 0 & S_{11}(3) & 0 \\ 0 & S_{11}(6) & 0 & S_{11}(8) \\ S_{11}(9) & 0 & S_{11}(11) & 0 \\ 0 & S_{11}(14) & 0 & S_{11}(16) \end{bmatrix},$$

$$\mathbf{S}_{11}^{2} = \begin{bmatrix} S_{11}(1) & 0 & 0 & S_{11}(4) \\ 0 & S_{11}(6) & 0 & 0 \\ 0 & 0 & S_{11}(11) & 0 \\ S_{11}(1) & 0 & 0 & S_{11}(16) \end{bmatrix}. \tag{3.19}$$

In the special case when only the zeroth-order harmonic is needed in the scattering matrix, the cascading approach becomes particularly efficient and simple. In fact, this situation forms the mathematical basis for the commonly used FSS equivalent circuits in which the FSS system is replaced by either a lumped inductance or a capacitance. From these equivalent circuits, the frequency response characteristics of a multilayered system can easily be predicted, and simple circuit theory can be used to design a system with the desired frequency variation. This special case also makes unequal-periodicity systems easy to handle, since the zeroth-order harmonic has no periodicity

dependence. This procedure, however, for the special case cannot always be applied. If it is determined that higher-order harmonics are required in the scattering matrix, then using the simple circuit approximations can lead to erroneous predictions of the critical points in the frequency response of the multilayered system.

## 3.3 RESULTS AND CONCLUSIONS

The authors have found that the following guidelines can be followed when selecting a method for analyzing multilayered FSS. First, if it is determined that only the zeroth-order harmonic is necessary in the scattering matrix, then the cascading approach should be employed, because, for this case, it would, by far, be the most accurate, simple, and efficient approach available. If, however, higher-order harmonics are required, then, if the multiscreen system is composed of two mirror-image-symmetric subsystems, the image screen technique should be utilized. Finally, if more than two subsystems are involved or if the multiscreen structure is not mirror image symmetric, then the scattering matrix approach should be used, after ensuring that an adequate number of harmonics have been included in the computation of the $S$-matrix. If two FSSs with nonsimilar periodicities are being cascaded together, then, in the instances where the periods are small whole-number multiples of each other, the $S$-matrix approach can easily be used. If, however, the periods are irrational or very large whole-number multiples of each other, then the $S$-matrix approach may prove to require too many harmonics in the matrix. These situations may not be accurately analyzable with the $S$-matrix approach.

It has been determined that a good rule of thumb for truncating a scattering matrix is to determine the lowest harmonic whose magnitude is less than $-22$ dB *and* for which no higher-order harmonic has a magnitude greater than $-22$ dB. The scattering matrix can be truncated at the harmonic that meets this criterion. All lower-order harmonics must be included in the $S$-matrix. If grating lobes appear in the scattered field, it is important to include them in the scattering matrix.

We now discuss a few interesting results obtainable with multiscreen techniques. Figure 3.9 shows layering of two strip gratings rotated by an angle $\Omega$ with respect to each other for $\Omega = 0°$, 45°, and 90°. This demonstrates how an FSS system can be used as a polarizer that gives a fair amount of control over the amplitudes of each of the two polarizations. This example also gives rise to an interesting technique, unique to the scattering matrix approach. In the example of Figure 3.9, the scattering matrix of the top subsystem is computed in the usual fashion. However, the scattering matrix of the second subsystem is derived by using the same unit-cell geometry as in the first, with the rotation of the strip grating relative to the first provided by a rotation in the azimuthal angle of incidence, $\phi$ (i.e., when computing the scattering



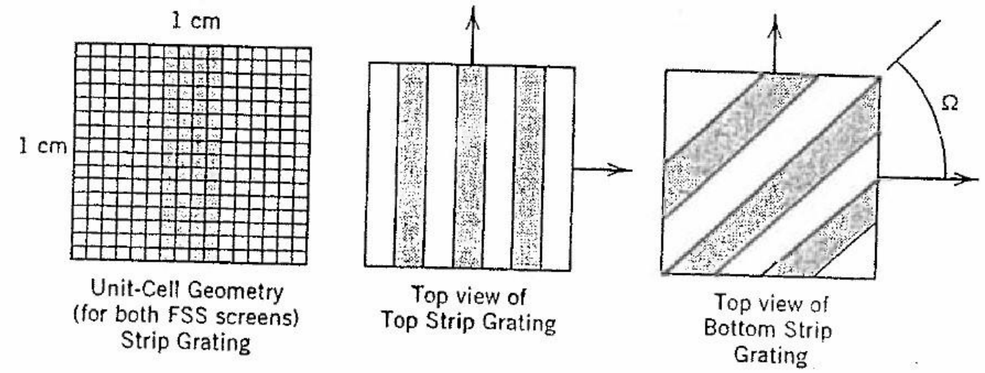


FIGURE 3.9 Effects of layering polarizers. Two freestanding ($\epsilon = 1$ everywhere) strip gratings are separated by 2 cm. The bottom screen is rotated by an angle $\Omega$ relative to the top screen: (a) $\Omega = 0°$, (b) $\Omega = 45°$, (c) $\Omega = 90°$.

matrix of the second subsystem, let $\phi = 90°$ for Figure 3.9(c)). In this way, the azimuthal rotation of two subsystems with respect to one another is accomplished by simply rotating the angle of incidence of one of the subsystems when computing its scattering matrix. This technique can be employed with any one- or two-dimensional system. Its advantage is that many multiscreen configurations can be studied even if the analytic capability of the

individual subsystems is limited to specific geometries, as would be the case if an entire-domain approach was used to study the FSS.

To demonstrate the effect of layering two unequal-periodicity systems, the example of Figure 3.10 is presented. For the one-dimensional case of Figure 3.10, the strip width is kept constant while the periodicities are allowed to vary. The scattering matrices of the individual subsystems were computed by using an entire-domain program that employs the Chebyshev polynomial and sinusoidal basis functions [9]. Each scattering matrix contained five harmonics. It can be seen that a certain amount of control over the level of the reflection coefficient can be obtained by varying the ratio of the two system periodicities.

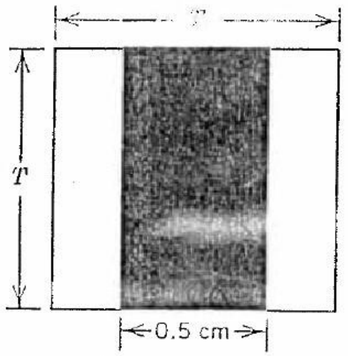


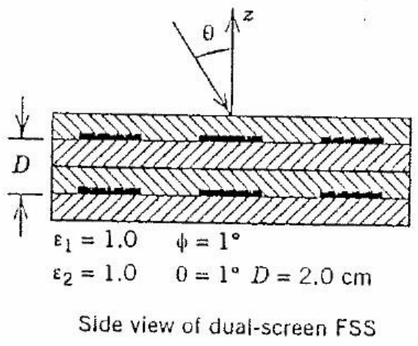


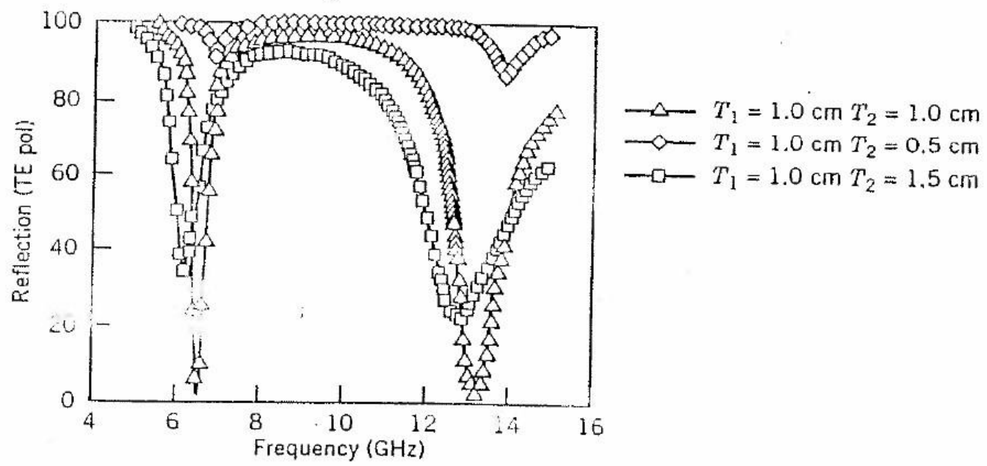


**FIGURE 3.10** Frequency response of a dual-screen one-dimensional FSS with unequal periodicity. In this case, the scattering matrices were computed by using entire-domain basis functions. The cascading technique is employed using five harmonics per scattering matrix.



As a final example, consider a dual-screen, four-frequency FSS (Figure 3.11) [4] proposed as a subreflector in a 4-m Cassegrain high-gain antenna, enabling simultaneous operation of the S (2.295 GHz), X (7.171 and 8.425 GHz), Ku (13.8 GHz), and Ka (32.0 and 34.5 GHz) bands. The X- and Ka-band feeds are located at the Cassegrain point and require that the FSS be reflective, whereas the S- and Ku-band feeds, located at the prime focus, require the FSS to be transparent. The two FSS screens have different unit-cell periodicities, with the bottom screen accommodating the S, X, and Ku bands, and the top screen (Ka-add-on) satisfies the Ka-band requirements. In this instance, from the −22-dB rule of thumb, it was found that, when the two FSS screens were separated by at least 0.5 in (air spacer; from 2 to 35 GHz), the simple zeroth-order scattering $S$-parameter matrix (a scattering matrix with only the zeroth-order harmonic) accurately modeled the dual-screen FSS. These results are shown in Figure 3.12 with comparisons with some measured results.

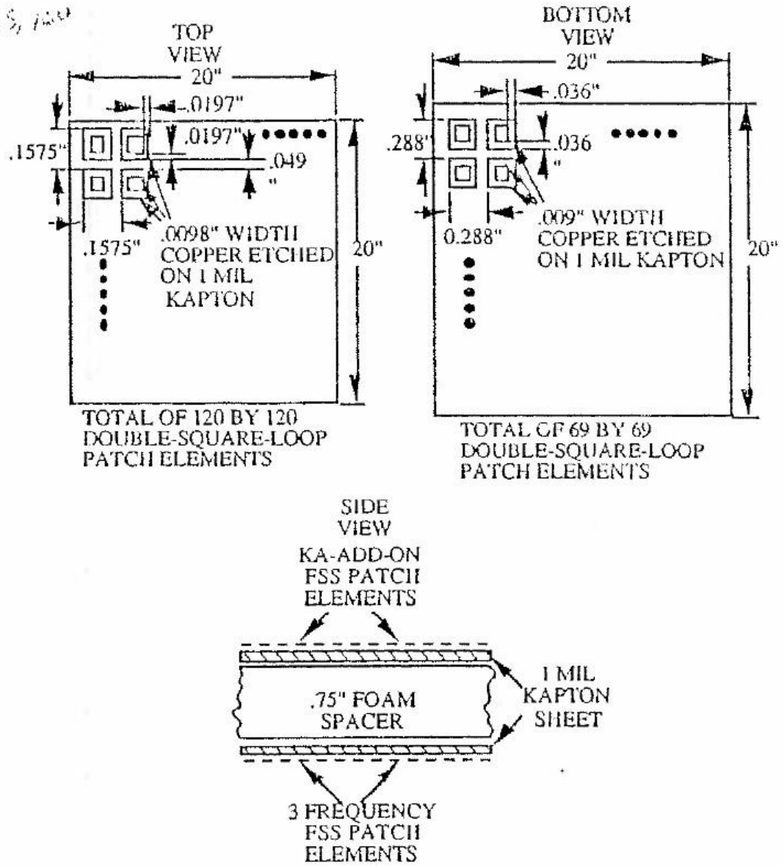


**FIGURE 3.11** Geometry of the dual-screen four-frequency FSS.

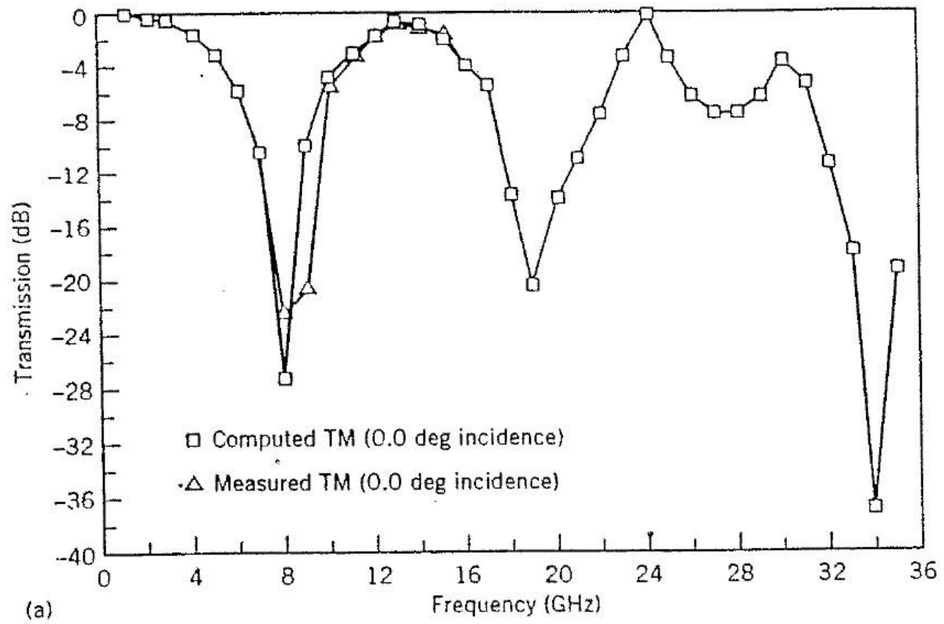


FIGURE 3.12 Comparison between measured and computed transmission characteristics of the add-on dual screen FSS design: (a) 0.0° TM incidence, (b) 40° TE incidence.



## REFERENCES


1. C. C. Chen, Diffraction of electromagnetic waves by a conduction screen perforated periodically with circular holes. *IEEE Trans. Microwave Theory Tech.* **MTT-19**(5), 475–481 (1971).
2. C. C. Chen, Transmission through a conducting screen perforated periodically with apertures. *IEEE Trans. Microwave Theory Tech.* **MTT-18**(9), 627–632 (1970).
3. T. A. Cwik, Scattering from general periodic screens. Ph.D. Dissertation, University of Illinois, Urbana (1986).
4. K. O. Merewether, Spectral-domain analysis of finite frequency selective surfaces. Ph.D. Dissertation, University of Illinois, Urbana (1989).
5. R. F. Harrington, *Field Computation by Moment Methods*. pp. 5–9. Krieger, Malabar, FL, 1968.
6. R. Mittra, C. H. Chan, and T. Cwik, Techniques for analyzing frequency selective surfaces—a review. *Proc. IEEE* 76(12), 1593–1615 (1988).
7. T. Cwik and R. Mittra, The cascade connection of planar periodic surfaces and lossy dielectric layers to form an arbitrary periodic screen. *IEEE Trans. Antennas Propag.* **AP-35**(12), 1397–1405 (1987).
8. J. D. Vacchione and R. Mittra, A generalized scattering matrix analysis for cascading FSS of different periodicities. *Int. IEEE Antennas Propag. Symp. Dig.*, Dallas, TX, Vol. 1, pp. 92–95 (1990).
9. T. K. Wu, Double-square-loop FSS for multiplexing four (S/X/Ku/Ka) bands. *Int. IEEE Antennas Propag. Symp. Dig.*, London, Ontario, Canada, Vol. 3, pp. 1885–1888 (1991).

CHAPTER FOUR

# Multiband Frequency Selective Surfaces

T. K. WU, Jet Propulsion Laboratory, California Institute of Technology, Pasadena, California

Frequency selective surfaces (FSS) have been considered for multiband reflector antenna applications [1–8]. Typically, an FSS is employed for the subreflector, and the different frequency feeds are optimized independently and placed at the real and virtual foci of the subreflector. Hence, only a single main reflector is required for multifrequency operation. For example, the FSS on the high-gain antenna (HGA) of the *Voyager* spacecraft was designed to diplex S and X bands [1]. In that application the S-band feed is placed at the prime focus of the main reflector, and the X-band feed is placed at the Cassegrain focal point. Note that only one main reflector is required for this dual-band operation. Thus, tremendous reductions in mass, volume, and, most important, cost of the antenna system are achieved with the FSS subreflector. This chapter presents two case studies of FSS applications to advanced multiband communication antennas [3–8]. Various practical FSS designs are described in detail to give the reader as many examples as possible.

In the past, the cross-dipole patch-element FSS was used for subreflector design in the reflector antennas of *Voyager* [1], for reflecting X-band waves and passing S-band waves, and the Tracking and Data Relay Satellite System (TDRSS), for diplexing S- and Ku-band waves [2]. As mentioned in Chapter 1, the characteristics of the cross-dipole element FSS change drastically as the incident angle is steered from normal to 40°. Thus, a large band

*Frequency Selective Surface and Grid Array*, Edited by T. K. Wu
ISBN 0-471-31189-8 

separation is required to minimize the radio-frequency (RF) losses for these dual-band applications. This is evidenced by the reflection and transmission band ratio ($f_r/f_t$) being 7 : 1 for single-screens FSS [2] or 4 : 1 for double-screen FSS [1] with cross-dipole patch elements. Much closer band spacings and a bandwidth insensitive to the incident angle variation can be obtained with dipoles sandwiched between dielectrics about $\lambda/2$ thick [9]. However, if a lighter-weight structure or circular polarization is required, then thin dielectrics supported by low-mass material must be used, and other elements have to be sought.

Thus, the first case study is to describe the gridded square-loop FSS development for a ground station reflector antenna used in orbiting very long baseline interferometer (OVLBI) applications. OVLBI is a new branch of radio astronomy, involving extension of the VLBI technique to include radio telescopes placed in orbit around the earth. Typically, VLBI involves simultaneous observations for widely separated radio telescopes, followed by correlation of the signals received at each telescope in a central processing facility. VLBI has been an important technique in radio astronomy for over 20 years because it produces an image whose angular resolution is far higher than that of any other technique.

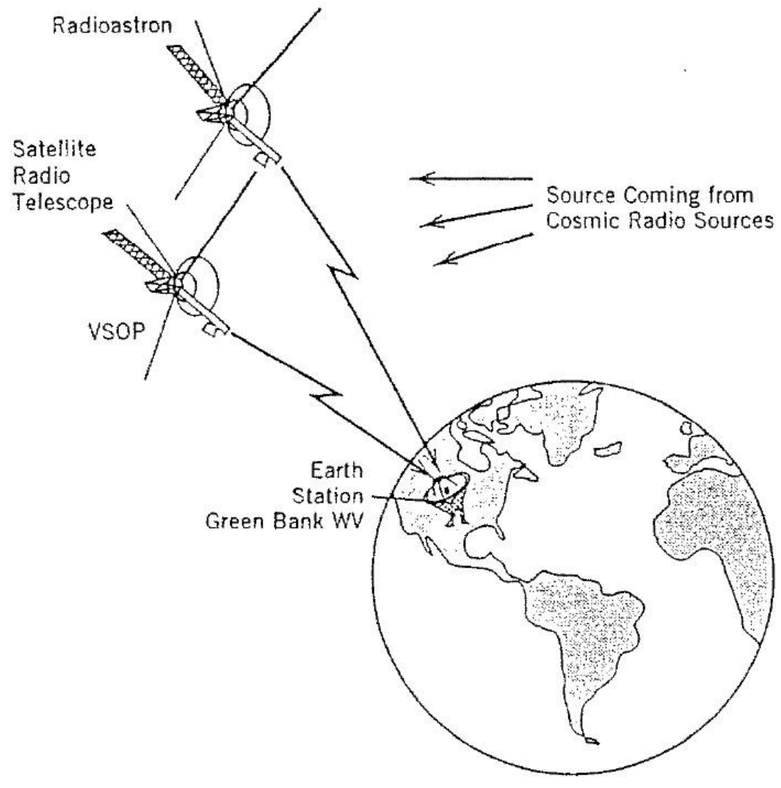


FIGURE 4.1 Scenario of orbiting very long baseline interferometry (OVLBI).



TABLE 4.1. OVLBI Reflector Antenna Requirements

| Frequency (GHz) | Bandwidth (GHz) | Usage | Polarization |
|---|---|---|---|
| 7.22 | 0.045 | *RADIOASTRON* uplink | LHCP |
| 8.47 | 0.1 | *RADIOASTRON* downlink | RHCP |
| 14.2 | 0.1 | VSOP downlink | LHCP |
| 15.3 | 0.1 | VSOP uplink | LHCP |

Currently, the National Radio Astronomical Observatory (NRAO) of the United States is constructing an earth station at Green Bank, West Virginia, to communicate with two QVLBI satellites: the Russian *RADIOASTRON*, and the Japanese VLBI Space Observatory Project (VSOP), as illustrated in Figure 4.1. The frequency allocations for the communication between this earth station and the two satellites are in the X and Ku bands, as described in Table 4.1. To meet this dual-band communication requirement, the multireflector antenna with a flat-panel FSS or dichroic, as shown in Figure 4.2, has been proposed. In this configuration, the flat FSS should be designed to reflect Ku-band signals (13.5–15.5 GHz) and to pass X-band signals

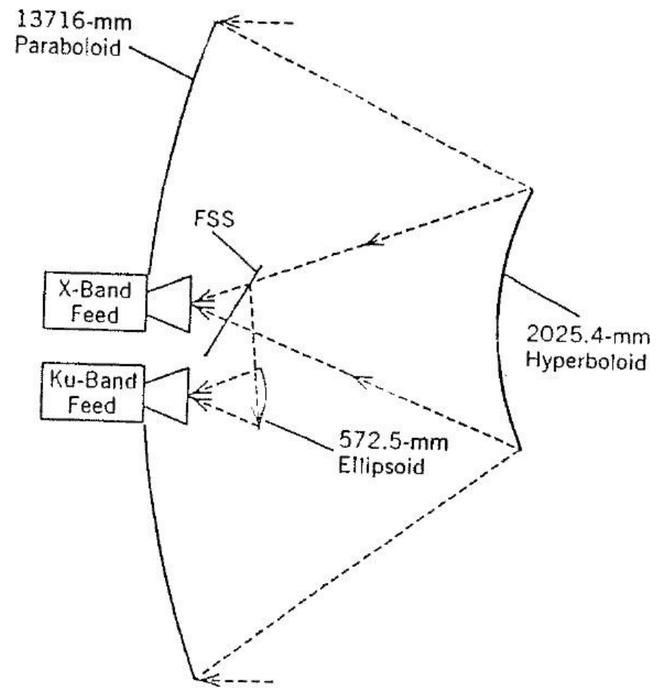


FIGURE 4.2 OVLBI earth station reflector antenna configuration (drawing not to scale).

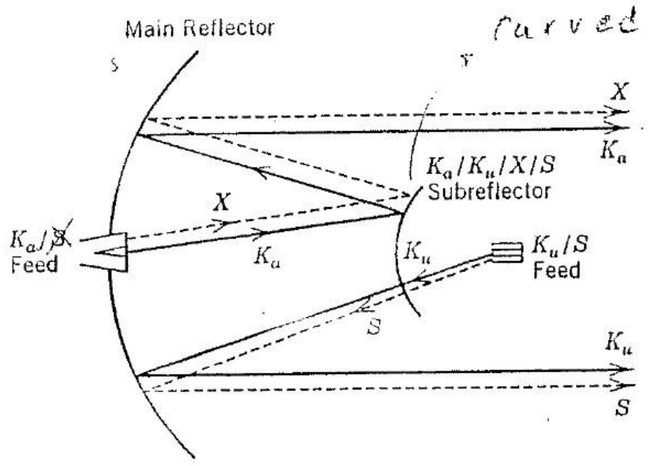


FIGURE 4.3 Proposed Cassini high-gain antenna with a four-frequency FSS.

(7–9 GHz). The reflection and transmission frequency band separation is $f_r/f_t = 14.5/8.0 = 1.8$. Because the satellite link is in circular polarization, the FSS must have similar responses to left- and right-hand circular polarizations (LHCP and RHCP) and, by extension, to transverse electric (TE) and transverse magnetic (TM) incidence. To reduce the antenna's noise temperature, one should minimize the RF insertion loss (including the ohmic loss) of the FSS for incident angles from normal to 40°.

Frequency selective surfaces with gridded square-loop patch elements [3, 10] have been designed for frequency band ratios from 1.5 to 2. Their resonant frequencies are fairly stable with respect to changes in incident angle and polarizations. In addition, the grid geometry is symmetrical in the $x$ and $y$ directions. This implies that it is also good for circular polarizations. The details of this FSS development are given in Section 4.1.

The second case study presented is the multiband FSS with double-loop elements for NASA's Cassini mission. NASA initiated a deep-space program named Cassini to explore the Saturnian planet system. Its spacecraft, scheduled to be launched in 1997, requires multiple RF frequencies at the S, X, Ku, and Ka bands for science investigations and data communication links. A single HGA with an FSS subreflector, as depicted in Figure 4.3, was proposed. This arrangement allows a Cassegrain configuration at the X (7.2 and 8.4 GHz) and Ka (32 and 34.5 GHz) bands and a prime focus configuration at the S (2.3 GHz) and Ku (13.8 GHZ) bands. The S and Ku bands are used for science investigation, and the X and Ka bands are used for deep-space telecommunication. Note that the Ku-band frequency is used for a close-encounter science application, such as radar mapping the surface of Titan (the largest moon of Saturan). Table 4.2 summarizes the RF requirements for this Cassini FSS.

TABLE 4.2. Cassini FSS Requirements

| Frequency (GHz) | Bandwidth (GHz) | Polarization | Pass/Reflect |
|---|---|---|---|
| 2.295 | 0.01 | Linear | P |
| 7.171 | 0.05 | Circular | R |
| 8.425 | 0.05 | Circular | R |
| 13.8 | 0.1 | Linear | P |
| 32.0 | 0.2 | Circular | R |
| 34.5 | 0.2 | Circular | R |



Frequency selective surfaces with double square-loop (DSL) [11–13] and double-ring (DR) [4–6, 14–16] patch elements have been designed for $f_r/f_t$ ratios from 1.5 to 2. Their resonant frequencies are fairly stable with respect to changes in incident angle and polarizations. In addition, the grid geometry is symmetrical in the $x$ and $y$ directions. This implies that it is also good for circular polarizations. Hence, the DSL and DR patch elements were considered for the Cassini FSS design to achieve (1) multiplexing of four frequency bands, (2) smaller frequency band separations ($f_t/f_r < 1.7$), and (3) low sensitivity to incident angle variation and polarizations.

To meet the Cassini antenna subsystem's RF requirements, two design approaches as shown in Figure 4.4, are proposed. In addition, the FSS screen was bonded to a Kevlar honeycomb panel to meet the mechanical and thermal environmental requirements. The first approach, implementing single-screen design, uses only a single FSS grid to reflect the X- and Ka-band waves and to pass the S- and Ku-band waves. The second approach, imple-

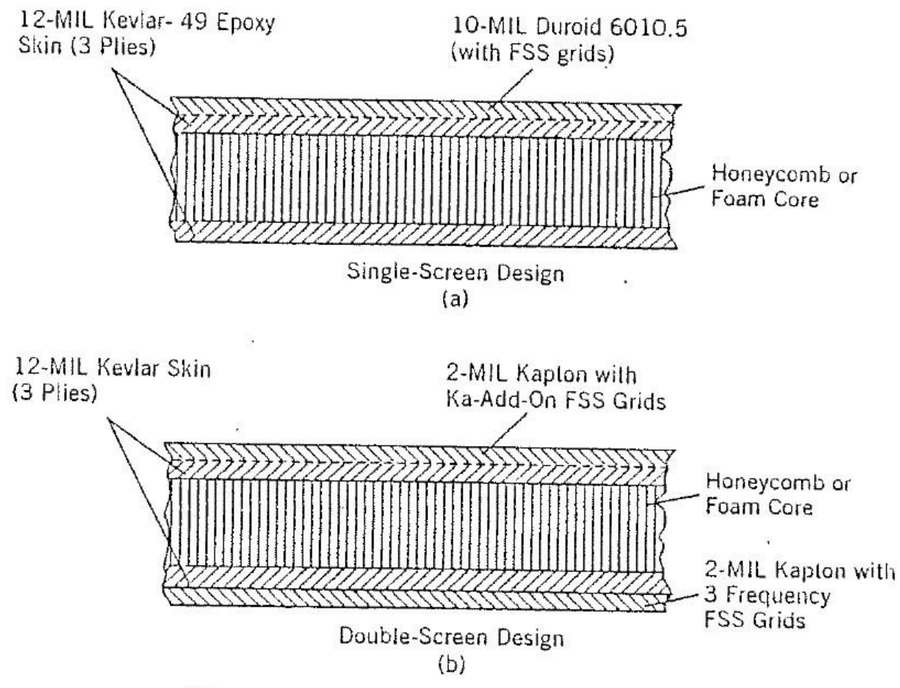


FIGURE 4.4 Cassini's FSS design approaches.

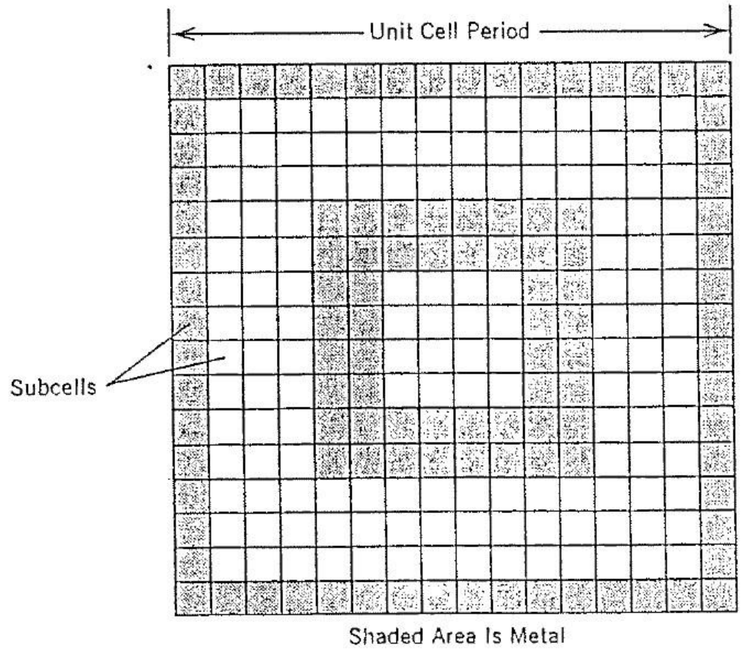


FIGURE 4.5 Construction of the subcell grid for a gridded square-loop patch element.

menting two-screen design, uses two FSS grids. The front FSS grid is called the Ka-add-on FSS. It reflects Ka-band waves but passes S-, X-, and Ku-band waves. The back FSS grid is called the three-frequency (or triband) FSS. It reflects X-band waves but passes S- and Ku-band waves. The resultant FSS reflects both X- and Ka-band waves but passes both S- and Ku-band waves. Several planar FSS breadboards with DSL or DR elements were developed based on these approaches and are described in detail in Section 4.2. Next, the evaluation of the integrated performance of a dual-reflector HGA with a curved FSS subreflector is presented.

## 4.1 DUAL-BAND FSS WITH GRIDDED SQUARE-LOOP ELEMENTS

The gridded square-loop FSS has been analyzed previously with the equivalent circuit model (ECM) [10]. But the ECM cannot accurately model the effects caused by the dielectric substrate and superstrate. Therefore, it was analyzed by the accurate integral equation technique (See Chapter 2). The analysis was implemented with the rooftop subdomain functions and by fitting the gridded square-loop element into the FSS's subcell grid (Figure 4.5). The FSS design and its transmission performances are described as follows.



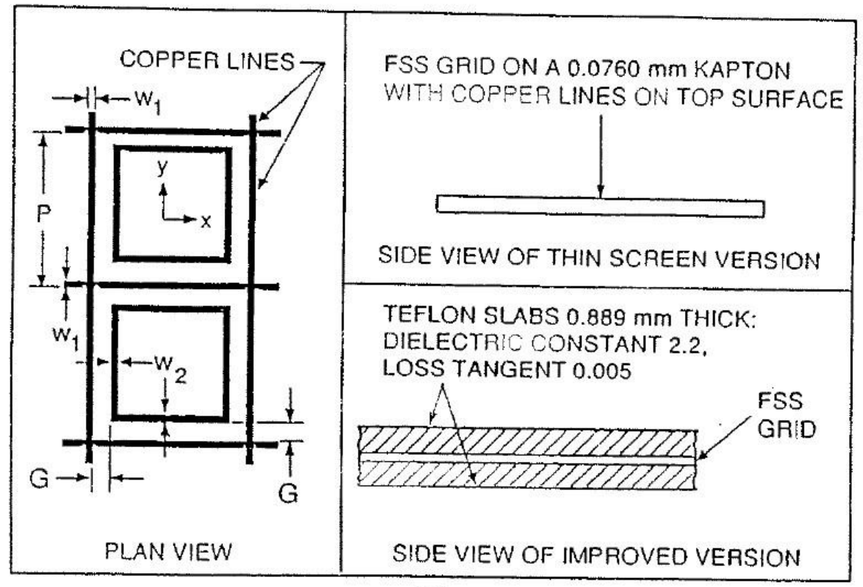


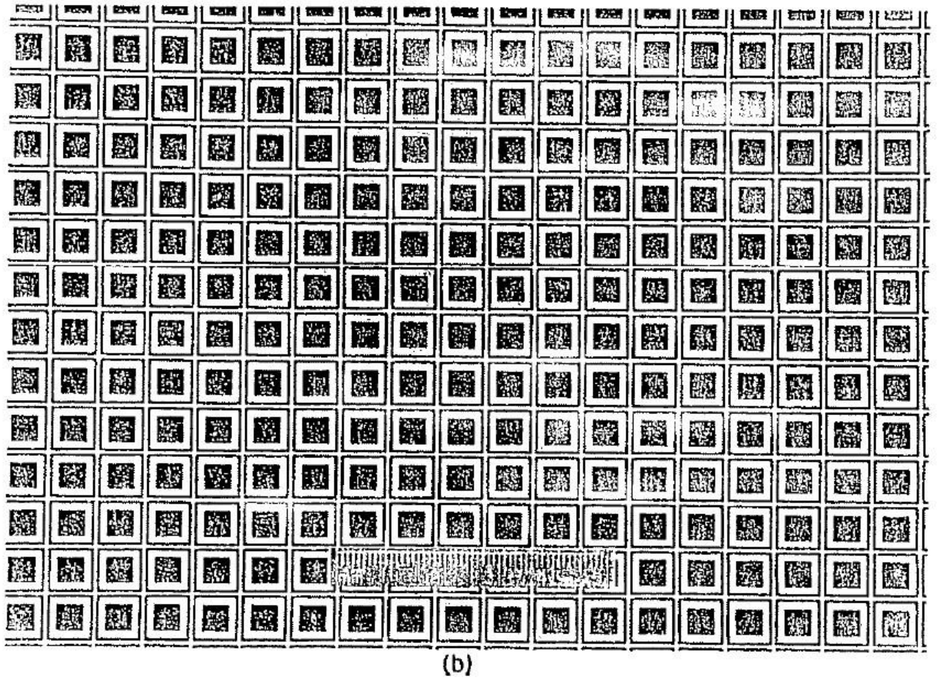


FIGURE 4.6 Gridded square-loop element FSS design configurations (a) and photo (b).

**TABLE 4.3. The Dimensions (mm) of Gridded Square-Loop FSSs**

| Design Type | $W_1$ | $W_2$ | $P$ | $G$ |
|---|---|---|---|---|
| Thin screen | 0.5588 | 1.125 | 8.999 | 0.5588 |
| Sandwiched | 0.4242 | 0.851 | 6.8 | 0.4242 |

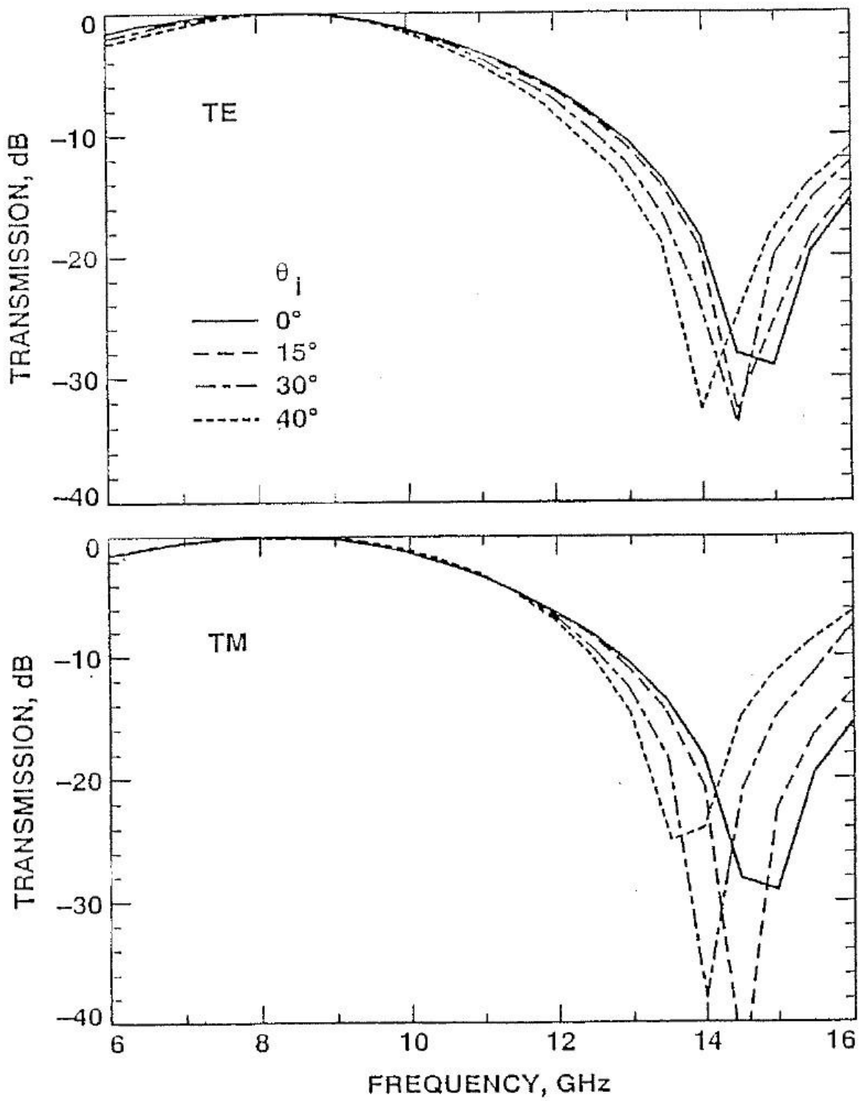


FIGURE 4.7 Predicted transmission performance of the thin-screen FSS.



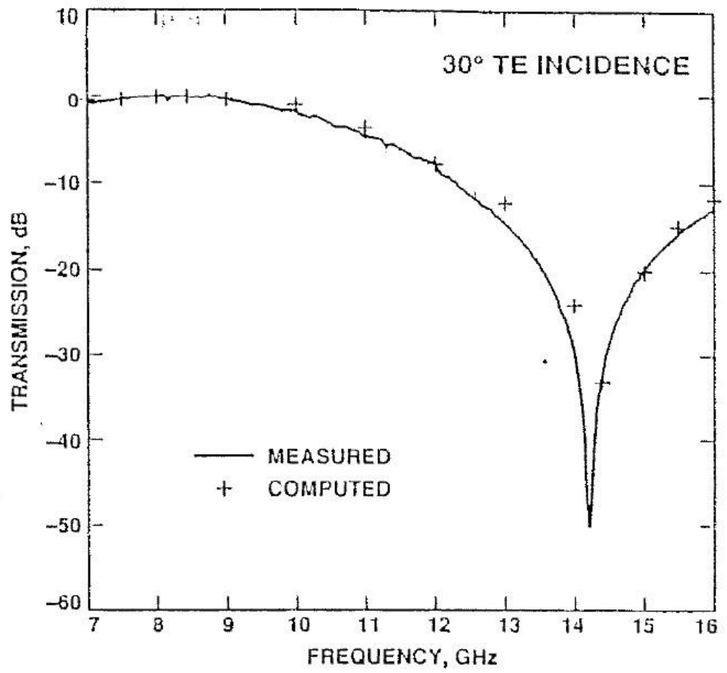


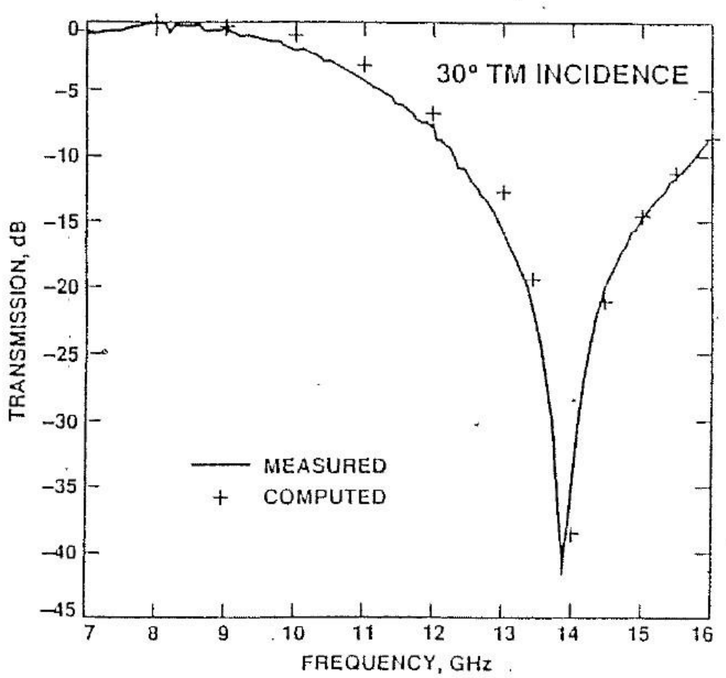


FIGURE 4.8 Comparison of the measured and computed transmission performance of the thin FSS.

TABLE 4.4. Computed Thin-Screen FSS Performance Loss (dB) Summary

| Frequency (GHz) | $\theta_i = 0°$ | 30° | | 40° | |
|---|---|---|---|---|---|
| | | TE | TM | TE | TM |
| 7.0 | .56 | .84 | .58 | 1.14 | .56 |
| 8.0 | .04 | .1 | .06 | .17 | .07 |
| 9.0 | .2 | .17 | .15 | .16 | .11 |
| 13.5 | .2 | .11 | .08 | .06 | .03 |
| 14.5 | .02 | .01 | .05 | .02 | .15 |
| 15.5 | .06 | .14 | .35 | .19 | .68 |

### 4.1.1 Thin-Screen Design Approach

For minimization of ohmic loss, the conducting gridded square-loop patches, as shown in Figure 4.6, were printed on a thin Kapton film (0.0762 mm thick, 3.5 dielectric constant, and 0.01 loss tangent). The grid dimensions are given in Table 4.3. This thin-screen FSS can be supported by a Fiberglass frame or by a rigid and RF-transparent foam block.

The predicted transmission performance of this thin-screen gridded square-loop FSS is illustrated in Figure 4.7 as a function of the incident angle

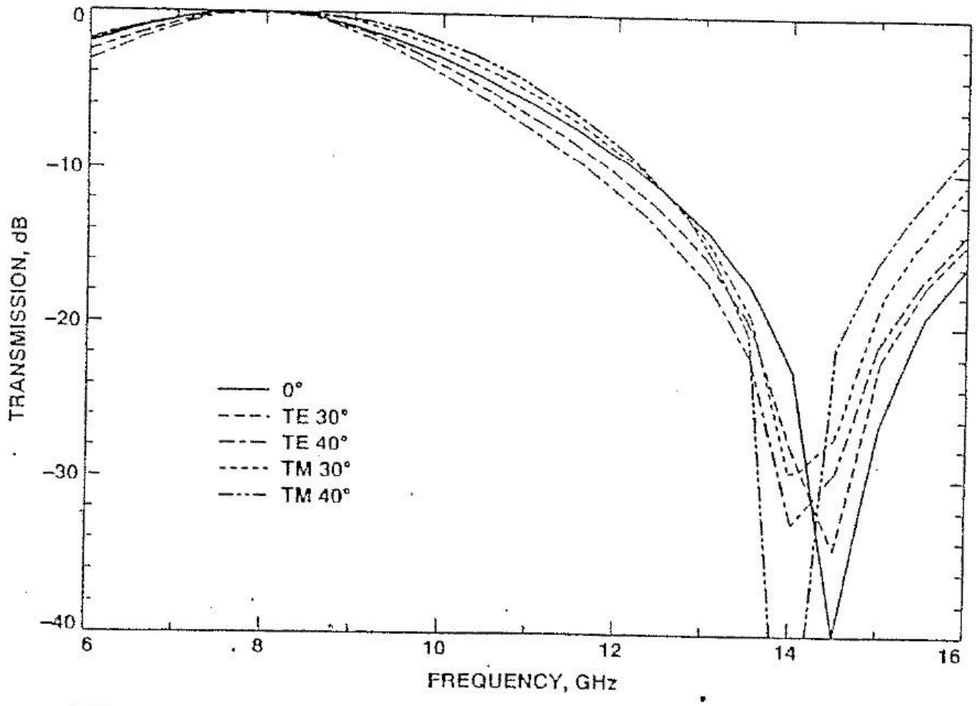


FIGURE 4.9 Predicted transmission performance of the sandwich FSS.



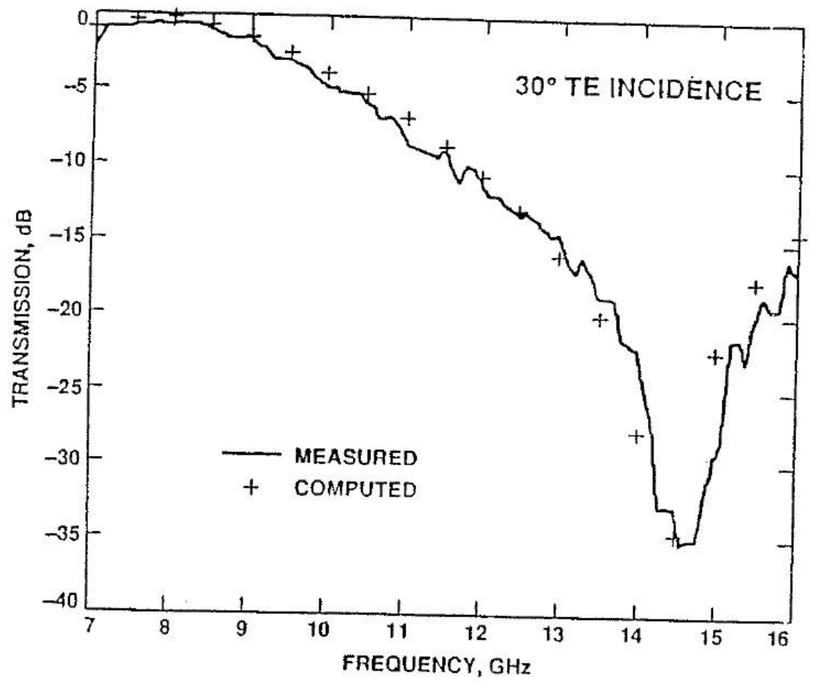


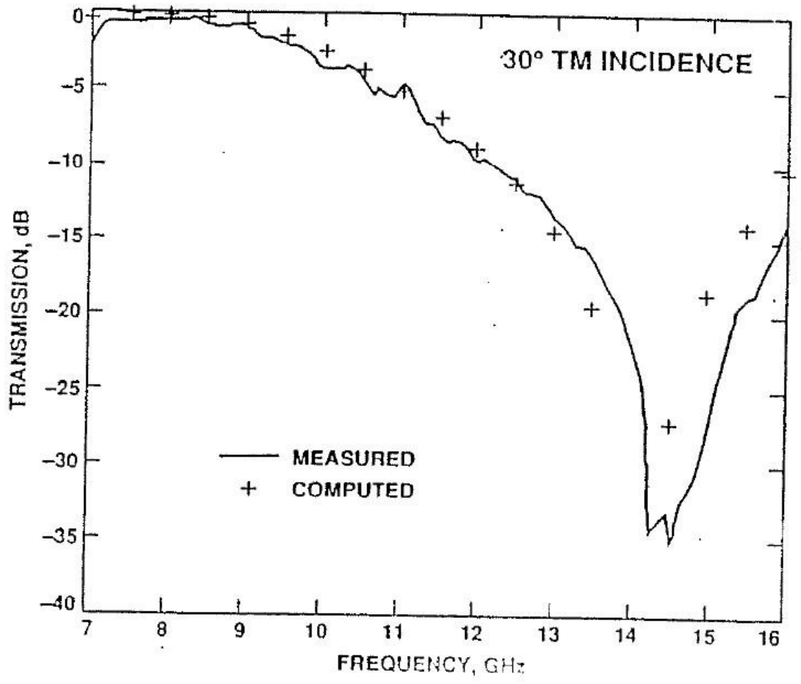


FIGURE 4.10 Comparison of the measured and computed transmission performance of the sandwich FSS.

TABLE 4.5. Computed Sandwiched FSS Performance Loss (dB) Summary

| | | 30° | | 40° | |
|---|---|---|---|---|---|
| Frequency (GHz) | $\theta_i = 0°$ | TE | TM | TE | TM |
| 7.0 | .52 | .75 | .57 | .998 | .58 |
| 8.0 | .04 | .04 | .03 | .04 | .04 |
| 9.0 | .77 | .87 | .51 | .998 | .35 |
| 13.5 | .14 | .09 | .12 | .06 | .1 |
| 14.5 | .02 | .02 | .02 | .02 | .03 |
| 15.5 | .05 | .08 | .14 | .09 | .25 |

and frequency for both TE and TM polarizations. Figure 4.8 compares the predicted and measured performance at $\theta_i = 30°$ with TE and TM polarizations. This verifies the gridded square-loop FSS's design approach as well as the accuracy of the design software. Table 4.4 summarizes the computed RF losses of this thin dichroic. The loss at 7, 8, and 9 GHz is the transmission loss, and the loss at 13.5, 14.5, and 15.5 GHz is the reflection loss. The FSS test panel size is 45.7 cm square.

### 4.1.2 Sandwiched Design Approach

Note in Figure 4.7 the resonant frequency shifts about 1.5 GHz as the incident angle is steered from normal to 40°. However, it was found that, by dielectrically loading the thin FSS, one can stabilize the resonant frequency drift due to variations in the incident angle and the field polarization. This was accomplished by sandwiching this thin screen between two low-loss Teflon slabs (with dielectric constant 2.2 and loss tangent 0.005), as illustrated in Figure 4.6. Since the resonance frequency shifts to a frequency lower than 14.5 GHz due to the dielectric loading, the grid dimensions must be scaled down, as listed in Table 4.3, to get the same 14.5-GHz resonant frequency for the sandwiched FSS. Figure 4.9 shows the predicted transmission performance when the grid is sandwiched between two 0.889-mm-thick Teflon slabs. Note that the resonant frequency shift for this new design is reduced to 1 GHz as the incident angle steered from normal to 40°. Figure 4.10 shows the good agreement between the predicted and measured results at $\theta_i = 30°$ with TE and TM polarizations. Transmission performance at other incident angles is summarized in Table 4.5.

## 4.2 MULTIBAND FSS WITH DOUBLE-RING OR DOUBLE-SQUARE-LOOP ELEMENTS

Considering the FSS design approaches of Figure 4.4, we describe the DR and, then, the DSL patch-element designs. Both single- and double-screen



FSS designs are presented to give the reader as many examples as possible. The FSS's RF performance strongly depends on the Kevlar honeycomb skin material's dielectric properties (i.e., the dielectric constant and the loss tangent). The material's dielectric property changes from one material to another and from one production batch to another. Most material vendors do not provide precisely the material's dielectric property. Two or more RF design iterations are necessary. Therefore, the design flow diagram of Figure 4.11 was implemented for FSS development.

### 4.2.1 Double-Ring Patch-Element FSS

Accurate integral equation (or modal) analysis for a DR-element FSS (Figure 4.12) is well documented in [4–6, 14–16]. Either a narrow or wide ring was used for the following DR FSS designs, depending on the width of the ring elements. The narrow-ring analysis is limited to ring elements with electrically small width, since it is based on the thin-wire approximation (i.e., no radial variation for the expansion function of the ring current). However, the wide-ring analysis is not limited, since it is based on the exact coaxial waveguide modal analysis. It was found [4, 6] that the narrow-ring approximation is usually valid for a ring width less than $0.025\lambda$, with $\lambda$ being the wavelength of the FSS's resonant frequency. In general, the narrow-ring FSS gives a higher-$Q$ (narrow bandwidth) performance than does the wide-ring FSS.

***Single-Screen Ka-Add-on (low-pass) DR FSS*** To design the required Ka-add-on FSS as shown in Figure 4.4b, we studied a single-screen FSS with an element consisting of one to four concentric rings. The goal is to determine a high-$Q$ ring-element FSS with maximum transmission loss for frequencies

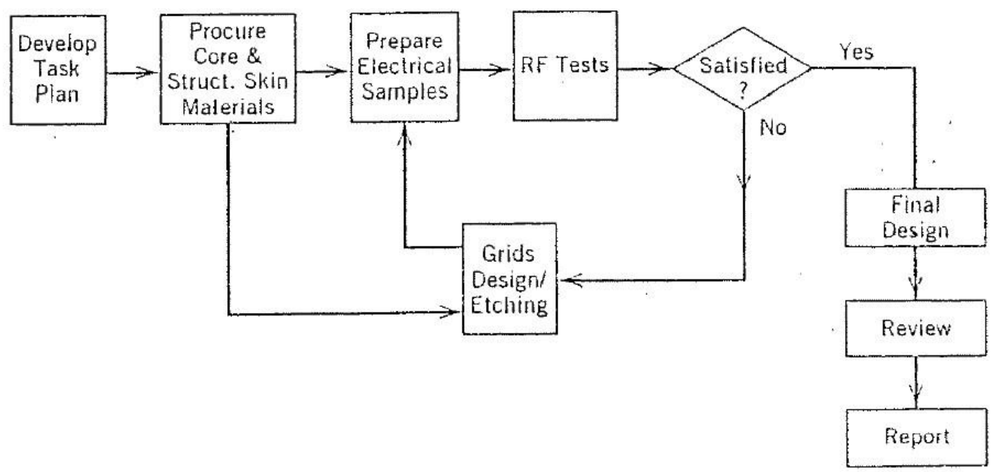


FIGURE 4.11 Cassini FSS design flowchart.

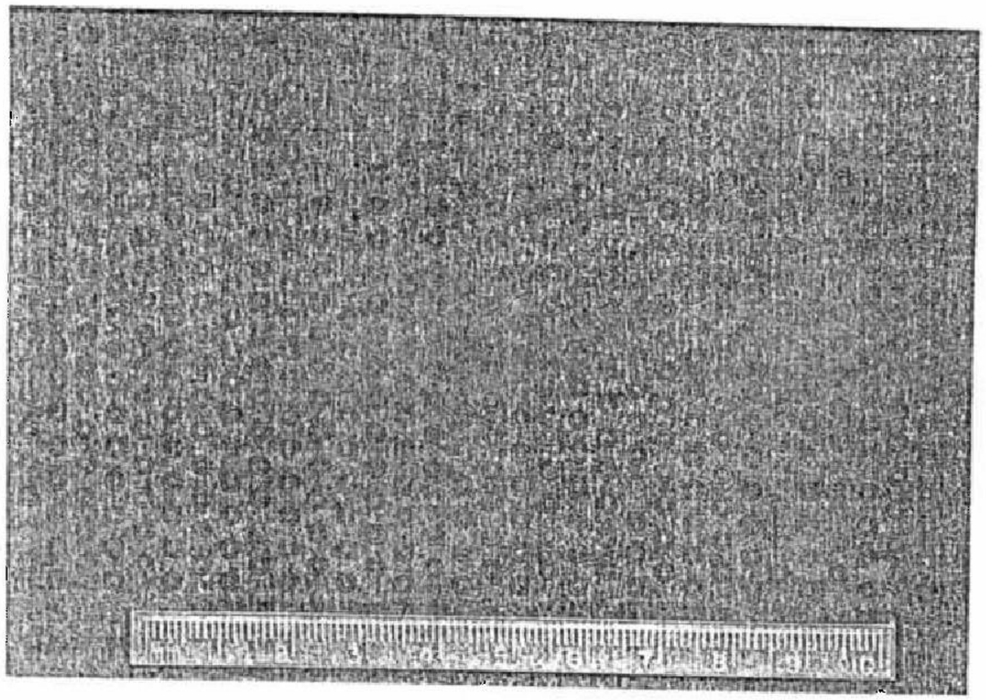

FIGURE 4.12 Photo of a double-ring patch-element FSS.




FIGURE 4.13 Design and transmission performance of the Ka-add-on DR FSS.



higher than 32 GHz and minimum transmission loss for frequencies lower than 14 GHz. As pointed out in Chapter 1, a freestanding single-ring element FSS will resonate at a frequency at which the ring's circumference is a wavelength. However, due to dielectric loading, this wavelength (or resonant frequency) is increased (or decreased) when the FSS grid is etched on a dielectric substrate. The frequency shift increases with increasing dielectric constant. Thus, the element's circumference should be reduced accordingly to reset the resonant frequency to 33 GHz.

Compared to single-ring-element FSSs, the DR-element FSS gives a much-higher-$Q$ performance [17] because it exhibits two resonances, one at a lower frequency (caused by the larger ring) and the other at a higher and closely separated frequency (caused by the smaller ring). Figure 4.13 gives the

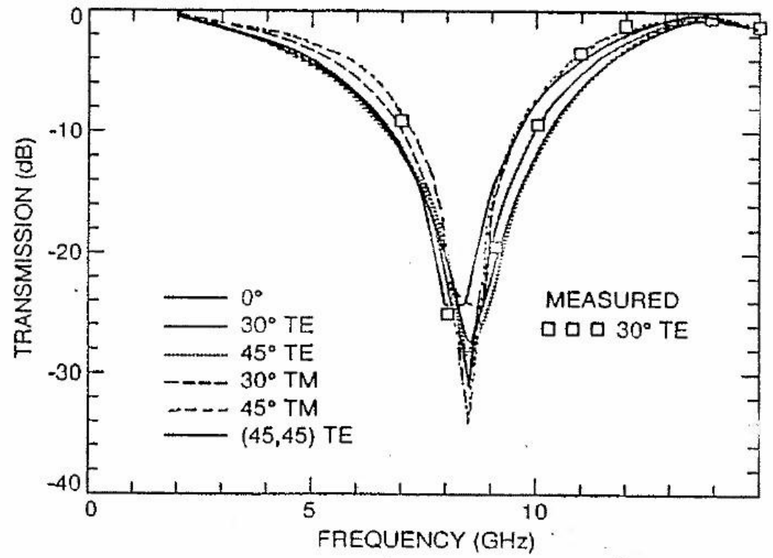


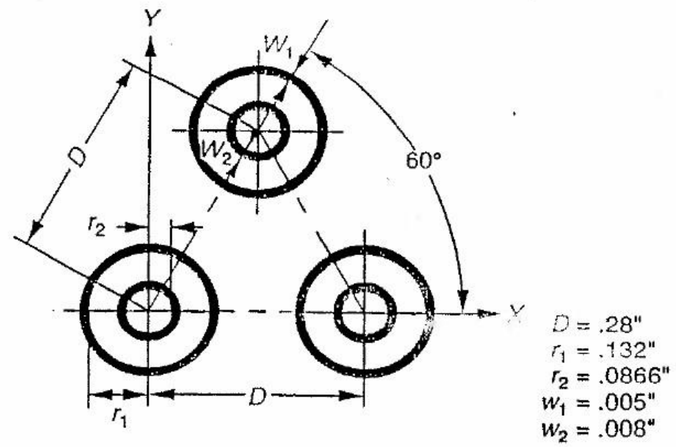


FIGURE 4.14 Design and transmission performance of the three-frequency DR FSS.

design and computed transmission performance of a DR FSS on the Kelvar honeycomb panel, as in Figure 4.4, for incident angles steered from normal to 45°. Note the DR patch-element array is etched on a 0.002-in-thick Kapton sheet with 0.029 oz/ft$^2$ copper and then bonded to the Kevlar honeycomb panel. Only representative measured data at 30° TE incidence are given here to demonstrate the good agreement between the computed and measured data. The computed results were obtained with the wide-ring code, because the narrow-ring code predicts a wrong resonant frequency. This also implies that the narrow-ring code is not valid for a ring width greater than $0.025\lambda$, where $\lambda$ is the wavelength at the resonant frequency of the FSS. Elements with more than two rings were also considered. However, they were discarded because of their fabrication complexity and no improvement in performance.

***Single-Screen Triband DR FSS*** By adjusting the second resonance frequency (or the smaller ring's geometry), we can design DR FSS to provide passband beyond the reflection band in addition to the lower passband. Hence, a single-screen triband FSS may be readily designed with the DR patch element. Figure 4.14 demonstrates this triband FSS design and performance. Again the DR patch-element array is etched on a 0.002-in-thick Kapton sheet with 0.029 oz/ft$^2$ copper and then bonded to the Kevlar honeycomb panel of Figure 4.4. Since the ring widths are small compared to the radii, the computed results may be obtained by narrow-ring or wide-ring FSS code. Only representative measured data at 30° TE incidence are given here to demonstrate the agreement between computed and measured data. As the figure shows, the resonant frequency is very close to the designated 8.4 GHz for both TE and TM polarizations even when the incident angle is changed from normal to 45°. The FSS's insertion losses at these three frequency bands are summarized in Table 4.6. Note that the losses at 2 and 14 GHz are transmission losses, whereas they are reflection losses at the other frequencies. The cross-polarized components are found to be more than 20 dB below the copolarized components.

**TABLE 4.6. RF Loss (dB) Summary of the Three-Frequency DR FSS**

| | | (30°, 0°) | | (45°, 0°) | |
|---|---|---|---|---|---|
| Frequency (GHz) | $(\theta_i, \phi_i) = (0°, 0°)$ | TE | TM | TE | TM |
| 2.0 | 0.5 | 0.57 | 0.4 | 0.72 | 0.27 |
| 7.0 | 0.25 | 0.5 | 0.61 | 0.46 | 1.0 |
| 8.5 | 0.14 | 0.12 | 0.16 | 0.11 | 0.17 |
| 14.0 | 0.26 | 0.29 | 0.28 | 0.36 | 0.24 |



***Single-Screen Four-Band DR FSS*** As mentioned, the DR-element FSS provides two resonances, one at a lower frequency (caused by the larger ring) and the other at a higher frequency (caused by the smaller ring). Therefore, one might be able to design a single-screen DR FSS for the Cassini four-band FSS. In other words, only one DR FSS grid might be needed for reflecting the X- and Ka-band waves while passing S- and Ku-band waves. To avoid the grating-lobe occurrence at the Ka band, one designs the single-screen FSS with a high-dielectric-constant ($\epsilon_r = 11$) Duroid 6010.5 substrate. In addition, the width of the inner ring must be large to provide a passband at the Ku band. Figure 4.15 shows the geometry and configuration of this DR FSS, and

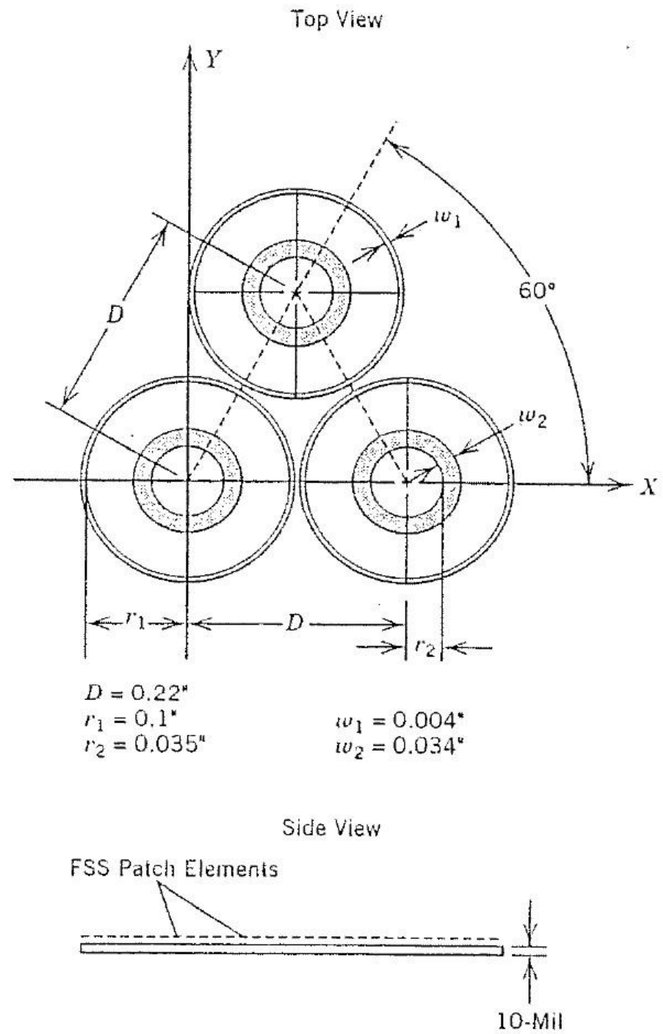


**FIGURE 4.15** Configuration of a double-ring FSS on a Duroid 6010.5 substrate.

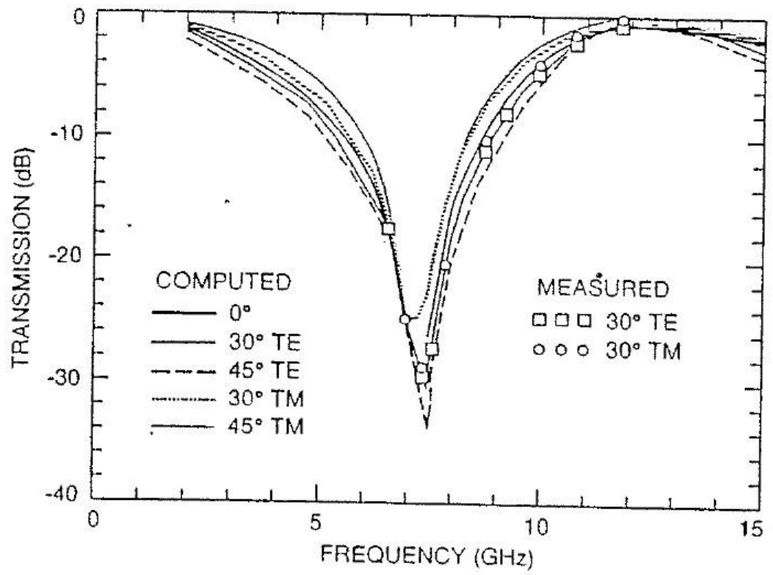


FIGURE 4.16 S-, X-, and Ku-band transmission performance of the FSS in Figure 4.15.

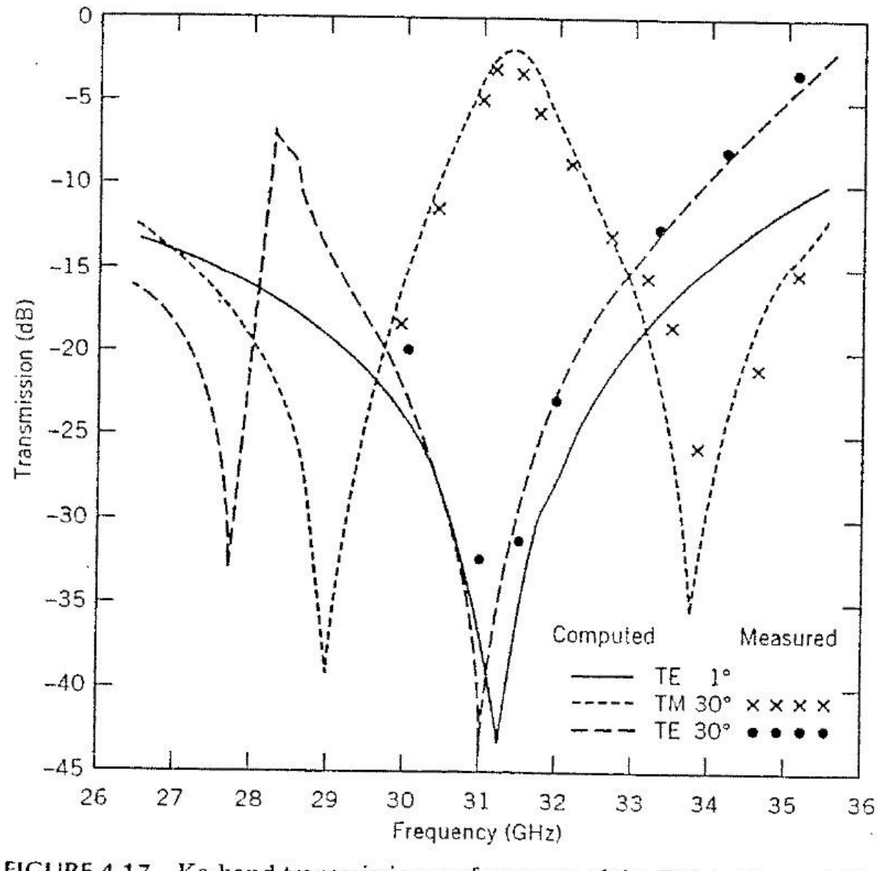


FIGURE 4.17 Ka-band transmission performance of the FSS in Figure 4.15.



its computed transmission performance is illustrated in Figure 4.16 at the S, X, and Ku bands for an incident angle steered from normal to 45°. Representative comparison data between the measured and computed results are also shown in Figure 4.16 for 30° incidence only.

The wide-ring code was used to compute the transmission performance of this single-screen DR FSS, since the inner ring width is much greater than $0.025\lambda$, with $\lambda$ being the wavelength of the second resonant frequency (33 GHz). The predicted Ka-band performance is illustrated in Figure 4.17 along with the representative measured results at 30° incidence. Figure 4.17 also shows that at the Ka band no common reflection band can be found for the TM and TE polarizations. This indicates that the single-screen DR FSS is good only for a three-frequency FSS application. For four-frequency FSS applications, the double-screen design should be implemented with this DR patch-element FSS.

***Double-Screen Four-Band DR FSS*** In Huang et al. [5], equations were derived to analyze single-screen or double-screen FSS with multiring patch elements. This analysis can be further extended to analyze an integrated double-screen FSS by employing the symmetry property and the technique of image theory [5]. In other words, the second FSS screen is the exact duplicate of the first. It was also stated that the second screen may be placed approximately a quarter-wavelength away from the first screen to reduce the reflection from each screen. But the reflections can be perfectly canceled at only one specific incident angle. As the incident wave is steered away from that designated angle, the performance deteriorates quickly.

To meet Cassini's four-band FSS requirements, one needs double-screen FSS with nonsimilar design [4, 6]; in other words, the element dimensions (especially the periodicity and the lattice types) are different for the two screens. As illustrated in Figure 4.4(b) this double-screen four-frequency FSS consists of a Ka-add-on FSS (element design shown in Figure 4.13) on the top side and a single-screen triband FSS (element design shown in Figure 4.14) at the bottom side of the honeycomb sandwich. Figure 4.18 shows the comparison of the computed and measured transmission performances for this double-screen FSS. The computed results were obtained by using the efficient single-mode cascading technique described in Wu and Lee [6] and in Chapter 3. The good agreement verified this efficient cascading approach. The double-screen FSS performance at all the Cassini frequencies is summarized in Table 4.7. The cross-polarized components are also found to be more than 20 dB below the copolarized components.

### 4.2.2 Double-Square-Loop Patch-Element FSS

In many aspects, the DSL FSS of Figure 4.19 has characteristics identical to the DR FSS. However, in the single-screen four-frequency FSS application to be described later, the DSL element was found to be better than the DR element. A DSL FSS etched on an electrically thin dielectric substrate can be

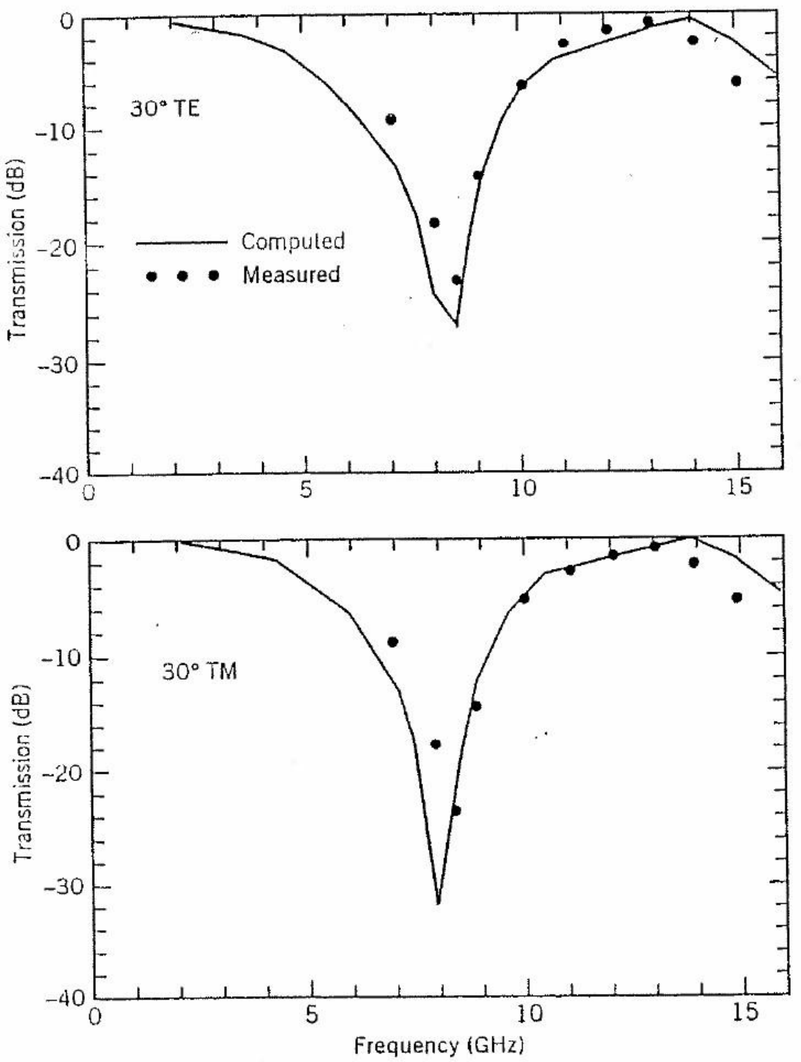


FIGURE 4.18 Transmission characteristics of the double-screen four-frequency FSS with 0.75-in-thick Kevlar honeycomb sandwich.

TABLE 4.7. RF Loss (dB) Summary of the Four-Frequency Double-Screen DR FSS

| | | (30°, 0°) | | (45°, 0°) | |
|---|---|---|---|---|---|
| Frequency (GHz) | $(\theta_i, \phi_i) = (0°, 0°)$ | TE | TM | TE | TM |
| 2.3 | 0.71 | 0.71 | 0.5 | 0.8 | 0.3 |
| 7.2 | 0.43 | 0.33 | 0.42 | 0.37 | 0.88 |
| 8.4 | 0.13 | 0.11 | 0.15 | 0.11 | 0.18 |
| 13.8 | 0.54 | 0.82 | 0.57 | 0.94 | 0.39 |
| 32 | 0.69 | 0.62 | 0.71 | 0.52 | 0.76 |
| 34.5 | 1.09 | 1.24 | 1.82 | 1.29 | 2.1 |



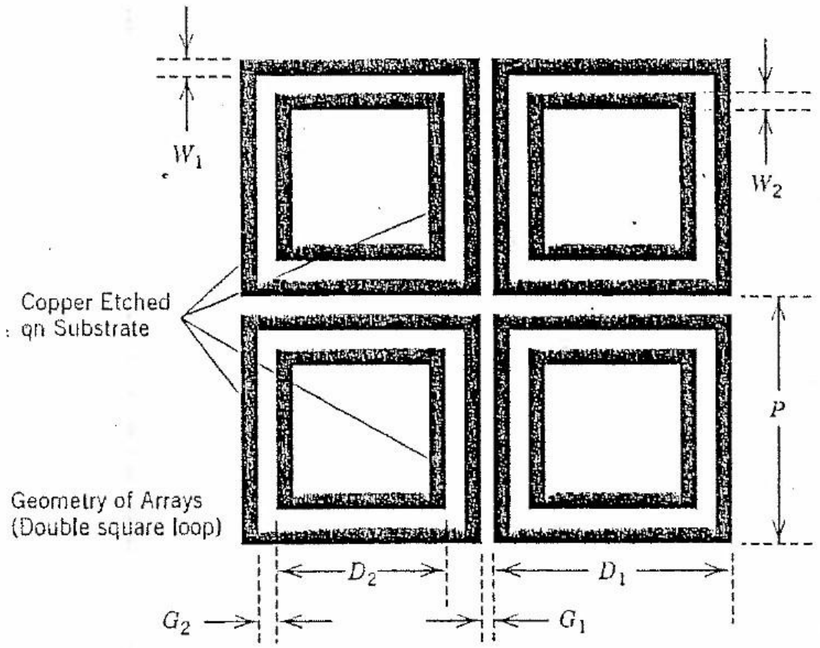


FIGURE 4.19 Configuration of a DSL patch-element FSS.

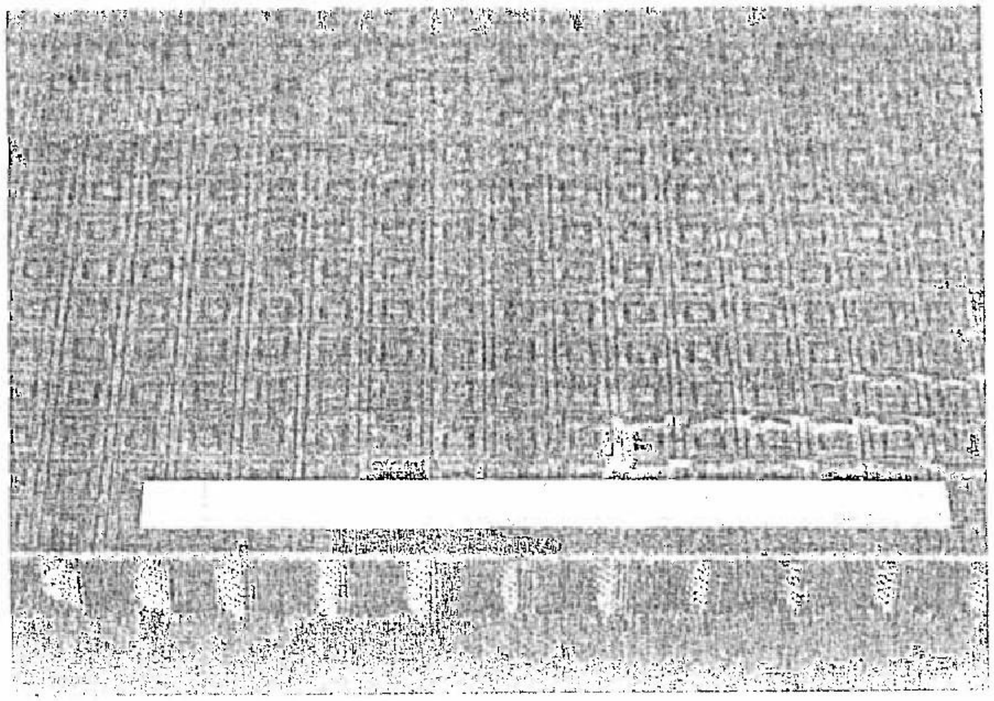

FIGURE 4.20 Triband DSL FSS with Kevlar honeycomb.

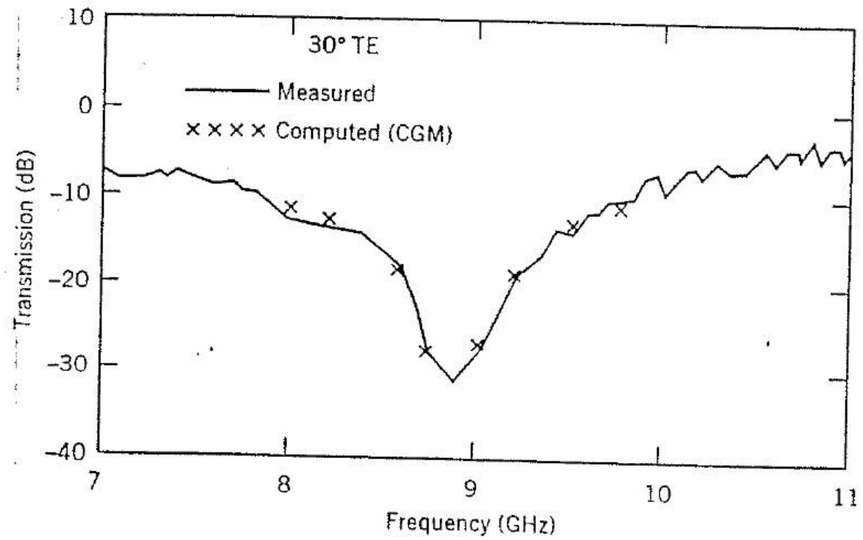


**FIGURE 4.21** Computed and measured transmission characteristics of a single-screen three-frequency DSL FSS with Kevlar honeycomb.

modeled by the ECM [12, 13]. Since the ECM does not accurately model dielectric effects, a DSL FSS on thick substrates should be analyzed by the integral-equation method described in Chapter 2.

***Single-Screen Triband DSL FSS*** A single-screen triband DSL FSS with a Kevlar honeycomb sandwich panel is shown in Figure 4.20. The FSS grids have a period of 0.311 in, and the elements are separated by a 0.041-in gap. The inner loop has a linewidth of 0.0307 in and is separated by a 0.0512-in gap from the outer loop, which has a linewidth of 0.0102 in. These grid dimensions were obtained by assuming the dielectric constant of the Kevlar/epoxy skin to be 3.5. However, after this DSL FSS was tested in the anechoic chamber, we found that the Kevlar/epoxy skin's dielectric constant must be 2.35 in order to get good agreement between measured and predicted results, as illustrated in Figure 4.21. Note that the resonance frequency is near 9 GHz instead of 8.4 GHz, since the Kevlar/epoxy skin's dielectric constant is 2.35 instead of 3.5.

Next a new DSL FSS was fabricated with the same Kevlar honeycomb sandwich panel, but all grid linear dimensions were scaled up by 5.3%. Figure 4.22 shows the predicted and measured transmission performances of this new FSS. Note that the resonant frequency for this new FSS is near 8.4 GHz for incident angles from normal to $(\theta_i, \phi_i = 45°, 45°)$ and for TE and TM polarizations. The measured data agree very well with the predicted data. Here only the representative normal incidence case is plotted. Table 4.8 summarizes the calculated loss performance of this scaled-up DSL FSS with Kevlar honeycomb.



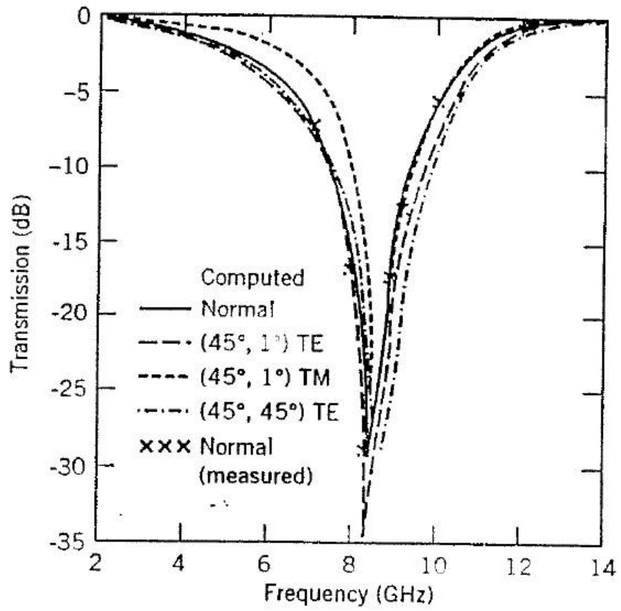


**FIGURE 4.22** Transmission performance of the scaled-up three-frequency DSL FSS.

***Single-Screen Four-Frequency DSL FSS*** In the previous section, the DSL FSS was designed for one reflection band (only the first resonance is stable enough for an application with a large variation of incident angle). However, with a careful design the DSL FSS should provide two resonances (or two reflection bands), one at a lower frequency (caused by the larger loop) and the other at a higher frequency (caused by the smaller loop). Therefore, one may be able to design a single-screen DSL FSS for the Cassini four-frequency FSS. In other words, only one DSL element FSS grid is needed for reflecting X- and Ka-band waves while passing S- and Ku-band waves. Similar to the DR FSS, the four-frequency DSL FSS was etched on a 0.01-in-thick Duroid 6010.5 substrate to avoid grating lobes.

The geometry and configuration of the four-frequency FSS with a Kevlar honeycomb are given in Figure 4.23. The figure also shows the computed and measured transmission data of this DSL element FSS for an incident angle

**TABLE 4.8. RF Loss (dB) Summary of the Three-Frequency DSL FSS**

| | | (30°, 0°) | | (45°, 0°) | |
|---|---|---|---|---|---|
| Frequency (GHz) | $(\theta_i, \phi_i) = (0°, 0°)$ | TE | TM | TE | TM |
| 2.3 | 0.38 | 0.46 | 0.28 | 0.58 | 0.19 |
| 7.2 | 0.24 | 0.96 | 1.41 | 0.8 | 2.1 |
| 8.4 | 0.1 | 0.17 | 0.16 | 0.15 | 0.23 |
| 13.8 | 0.13 | 0.18 | 0.12 | 0.36 | 0.1 |

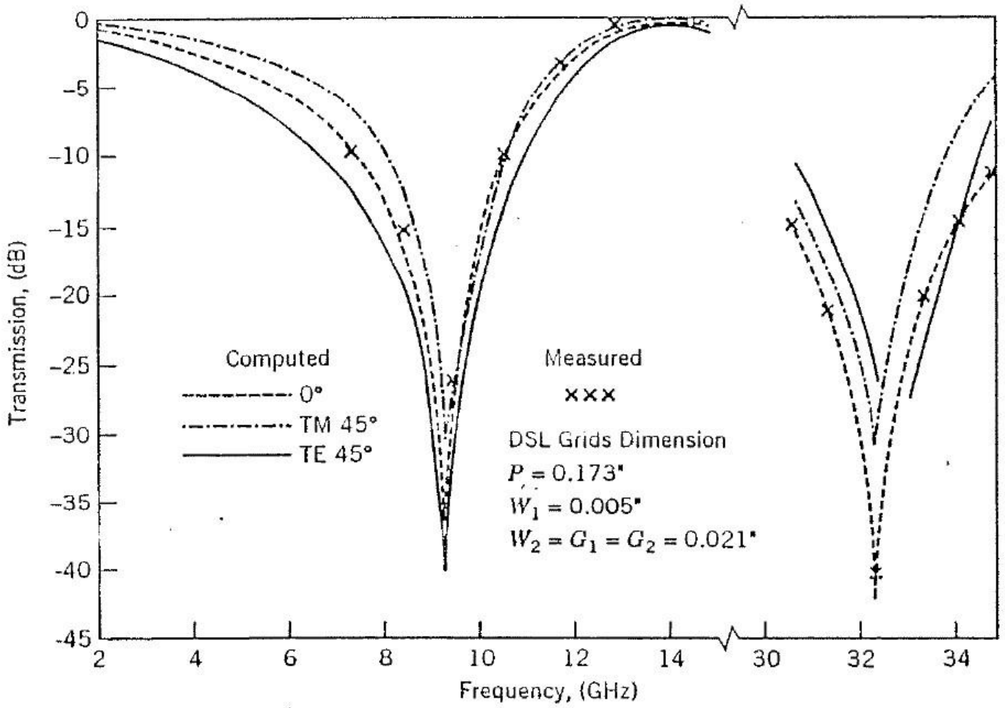


**FIGURE 4.23** Design and transmission performance of the single-screen four-frequency DSL FSS.

steered from normal to 45°. The resonant frequencies are very stable with respect to incident angle variation and are near the design frequencies, 8.45 GHz and 33 GHz. Only representative measured data at normal incidence are shown here. Good agreement between measured and predicted results is observed for incident angles at 0°, 30°, and 45° and for TE and TM polarizations. This verified the single-screen four-frequency FSS design approach. Table 4.9 summarizes the computed RF loss performance of this DSL-element FSS. Note in Section 4.2.1 we found that the single-screen four-frequency FSS cannot be designed with a DR element due to a higher-

**TABLE 4.9.** RF Loss (dB) of the Single-Screen Four-Frequency DSL FSS

| | | 30° | | 45° | |
|---|---|---|---|---|---|
| Frequency GHz | $\theta_i = 0°$ | TE | TM | TE | TM |
| 2.3 | .95 | 1.2 | .73 | 1.6 | .5 |
| 7.2 | .45 | .37 | .61 | .27 | .9 |
| 8.4 | .08 | .07 | .11 | .06 | .16 |
| 13.8 | .37 | .56 | .29 | .9 | .2 |
| 32 | .09 | .17 | .13 | .16 | .69 |
| 34 | .14 | .2 | .21 | .13 | .43 |



order moding problem in the Ka band. Therefore, we conclude that the DSL element is superior to the DR element for multiband ($\geq$ four bands) FSS applications.

The single-screen FSS has the advantages of lower mass, smaller volume, and easier fabrication over the double-screen approach, since neither accurate alignment nor a dielectric spacer with uniform thickness and dielectric properties is required. However, to ensure that this FSS operates at all frequency bands (i.e., from 2 to 35 GHz), we require a high-dielectric-constant ($\varepsilon_r \geq 11$) substrate for eliminating the grating lobe at 32 and 34 GHz. Currently, no high-dielectric-constant material (e.g., the Duroid 6010.5 laminate) has been qualified for space applications. Therefore, the following double-screen DSL FSS is considered for the Cassini four-frequency FSS.

***Double-Screen Four-Frequency DSL FSS*** The double-screen four-frequency DSL FSS consists of a Ka-add-on and a triband DSL FSS, similar to the double-screen DR FSS. The geometry of a single-screen Ka-add-on DSL FSS with the Kevlar honeycomb of Figure 4.4(b) is given in Figure 4.24. The

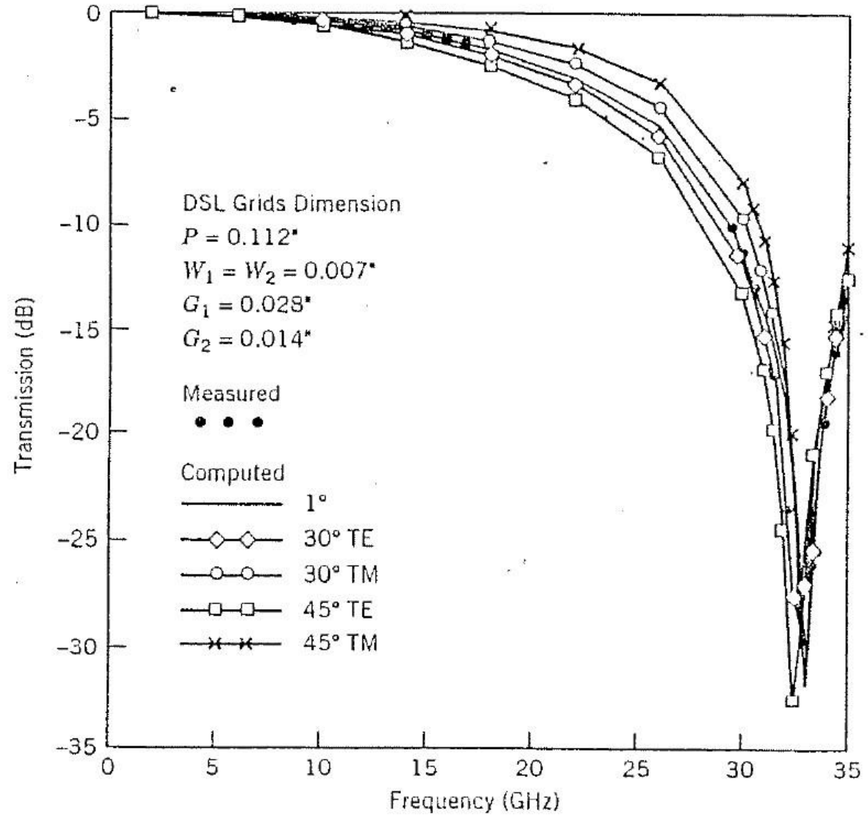


**FIGURE 4.24** Design and transmission performance of a single-screen Ka-add-on DSL FSS with Kevlar honeycomb.

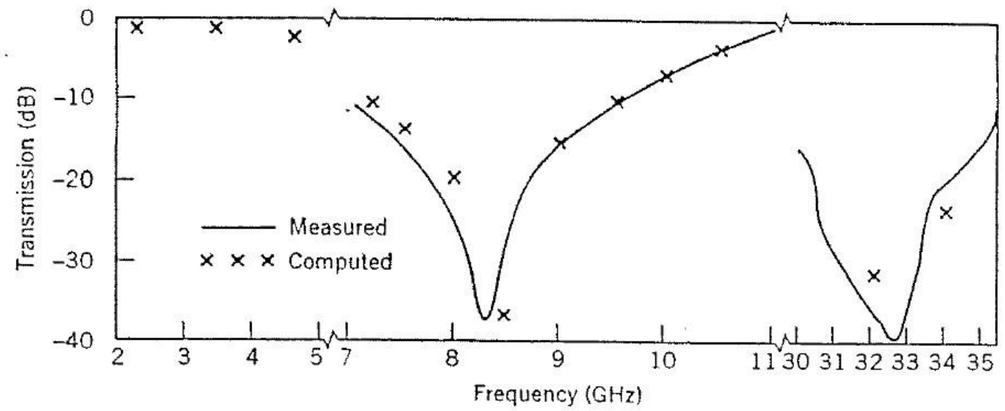


FIGURE 4.25 Comparison of computed and measured transmission performance of a double-screen four-frequency DSL FSS.

predicted and measured transmission performances are also plotted in Figure 4.24 for an incident angle steered from normal to 45° and for TE and TM polarizations. Figure 4.24 also illustrates the comparison between the computed and measured data for this FSS's transmission performance. Similar to the low-pass DR FSS, the good agreement between measured and calculated results validates this high-Q low-pass DSL FSS approach.

This DSL FSS (Figure 4.24) was then assembled with the three-frequency DSL FSS (Figure 4.22) to become a double-screen four-frequency FSS as shown in Figure 4.4(b). A representative comparison between the measured and computed transmission performances of this double-screen FSS is shown in Figure 4.25 at normal incidence. The computed RF loss performance is summarized in Table 4.10. This completes all the necessary Cassini FSS designs.

TABLE 4.10. RF Loss (dB) of the Double-Screen Four-Frequency DSL FSS with Honeycomb

| | | 30° | | 45° | |
|---|---|---|---|---|---|
| Frequency (GHz) | $\theta_i = 0°$ | TE | TM | TE | TM |
| 2.3 | .41 | .5 | .33 | .68 | .23 |
| 7.2 | .65 | .73 | 1.1 | .85 | 1.95 |
| 8.4 | .14 | .17 | .19 | .22 | .29 |
| 13.8 | 1.1 | 1.2 | .73 | 2.1 | .53 |
| 32 | .53 | .19 | .22 | .21 | .48 |
| 34 | .21 | .28 | .33 | .2 | .3 |



## 4.3 DUAL-REFLECTOR ANTENNA WITH FSS SUBREFLECTOR

Once the FSS element design is established, the next task is to estimate the integrated performance of the HGA/FSS as illustrated in Figure 4.3. In the past, the dual-reflector system's directivity was evaluated without the FSS effect; then the estimated FSS loss was subtracted from this directivity to obtain an approximate directivity for the HGA/FSS system [2]. Many factors, such as surface curvature, different incident angle/polarization, and phase-front distortion of the FSS subreflector, are not considered in this approach, but they are very important for accurately predicting the reflector system's sidelobe and cross-polarization levels.

Often it is necessary to incorporate in the HGA pattern computational model the FSS subreflector's transmitted/reflected field variation in polarization and incident angle with respect to local coordinates. It is also assumed that the local transmitted/reflected fields of the subreflector are available based on the planar FSS model. An FSS transmission/reflection coefficient table is computed with TE and TM polarizations at various incident angles. This FSS table is an expanded tabulation of the FSS's transmission and reflection coefficients at various incident angles $(\theta_i, \phi_i)$ and at a specified frequency. Next, either the physical optics (PO-PO) method [18] or the hybrid geometric optics and physical optics (GO-PO) technique [4] may be implemented with this FSS table to compute the dual-reflector radiation pattern. In this section the efficient hybrid GO-PO technique is implemented.

In the GO-PO analysis of a dual-reflector antenna with an FSS subreflector, the following steps are used to evaluate the effect of the FSS on the reflector anntenna's performance. First, the ray path is determined starting from the feed through the subreflector to a grid point on the main reflector's aperture plane. This leads to an evaluation of the angles at which the ray is incident on the FSS subreflector and the point of intersection. A local coordinate system is also determined at this point of intersection. The incident field is then decomposed into local TE and TM components. The reflected or transmitted fields through the subreflector are next computed by simple multiplications of the incident fields and the FSS's reflection/transmission coefficients, which are efficiently calculated by linearly interpolating the FSS table. Once the main reflector's aperture field variation caused by the FSS subreflector is determined, the far-field pattern and the directivity of the dual reflector are readily computed via an efficient FFT technique.

Consider the HGA/FSS system of Figure 4.3. Here we assume the FSS is composed of the double-screen four-frequency DR FSS as in Section 4.2.1. The main dish is a 12-ft-diameter parabolid with $F/D = 0.3377$, and the FSS subreflector is a 17.25-in-diameter hyperboloid with eccentricity 1.5. All the Cassegrain feeds are assumed to have a $\cos^{22.5}\theta$ pattern, whereas the prime focus feeds have a $\cos\theta$ pattern. The computed far-field patterns with and without the FSS are given in Figures 4.26(a–f) for frequencies at 2.3, 7.2, 8.4, 13.8, 32, and 34.5 GHz, respectively. As expected, the side-lobe and

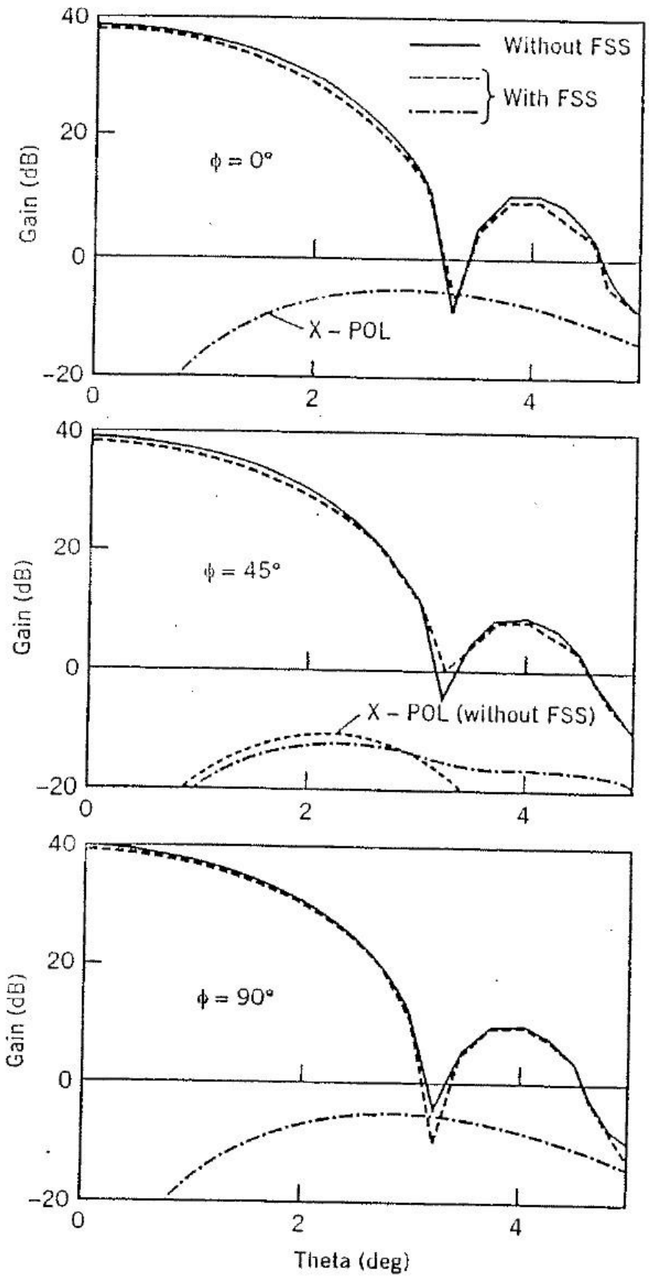


FIGURE 4.26(a) Far-field pattern of the HGA/FSS at 2.3 GHz.



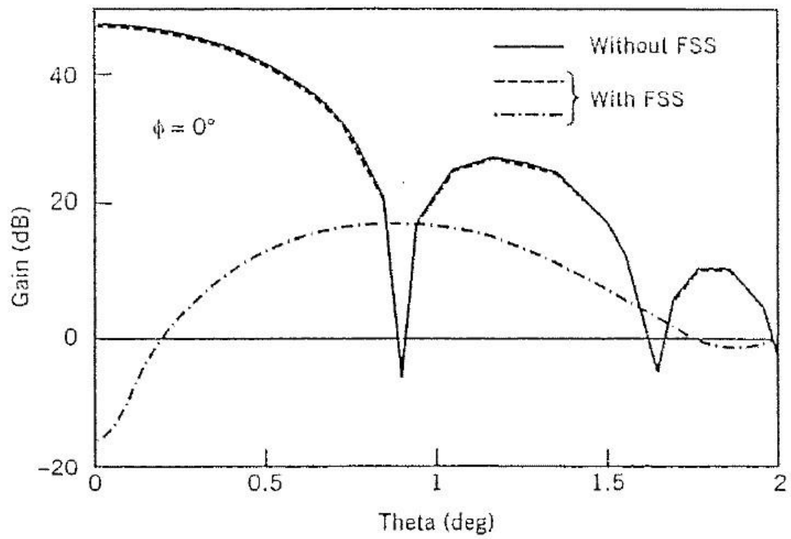


FIGURE 4.26(b) Far-field pattern of the HGA/FSS at 7.2 GHz.

cross-polarization levels are higher with the presence of the four-frequency FSS. The directivity is reduced with the FSS and is summarized in Table 4.11. It shows that the directivity reduction due to FSS insertion loss is less than 1 dB for all in-band frequencies except 34.5 GHz. Although the transmission loss of the planar FSS at 13.8 GHz changes from 0.54 to 0.94 dB for various incident angles, the dual-reflector's directivity decreases by only

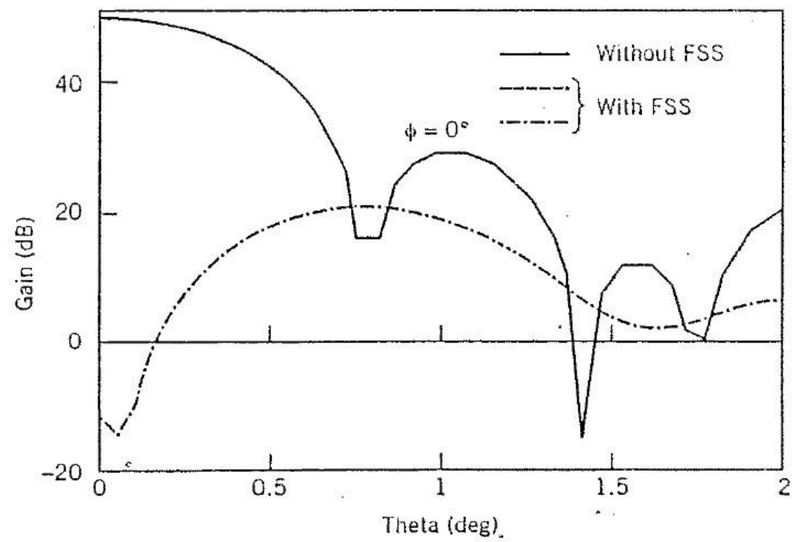


FIGURE 4.26(c) Far-field pattern of the HGA/FSS at 8.4 GHz.

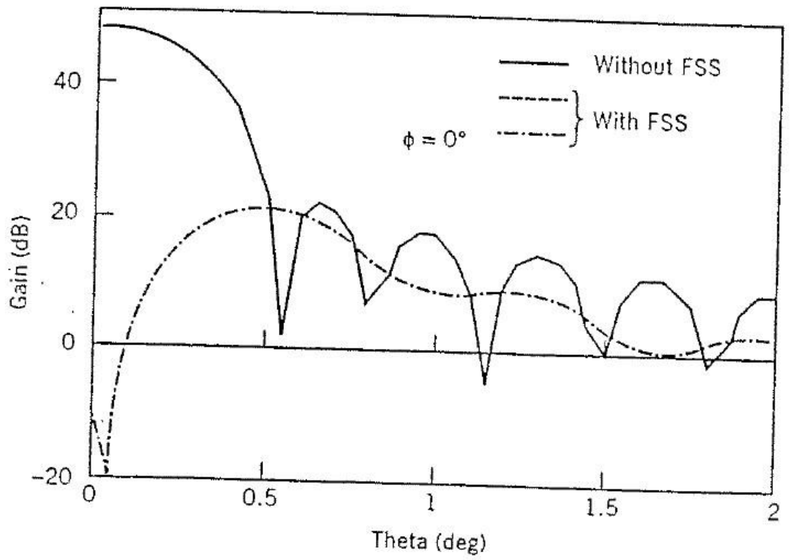


FIGURE 4.26(d) Far-field pattern of the HGA/FSS at 13.8 GHz.

0.2 dB with the FSS. The side-lobe level is about the same with and without the FSS. This effect is mainly due to the main dish's high edge taper caused by the high-FSS transmission loss that occurs at large incident angles. It also indicates that occasionally the reflector's aperture field variation caused by the FSS yields good directivity and sidelobe performance. Furthermore, this hybrid GO-PO method has the capability of including the diffracted fields

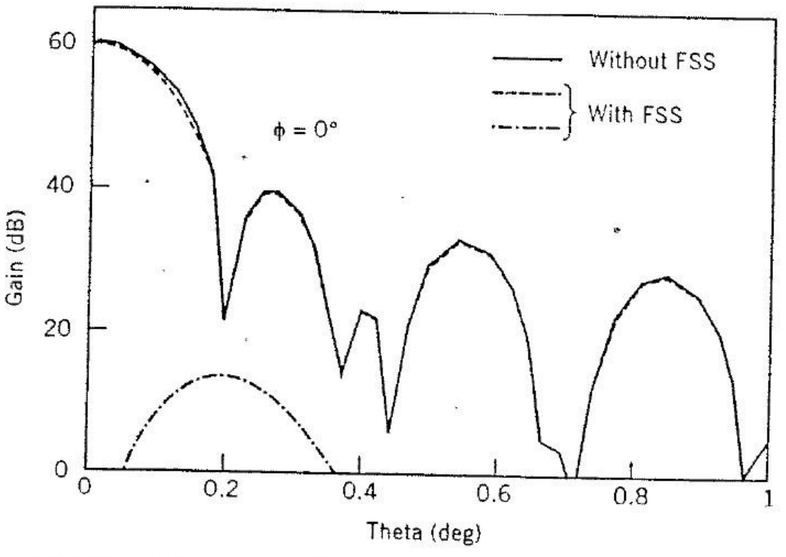


FIGURE 4.26(e) Far-field pattern of the HGA/FSS at 32 GHz.



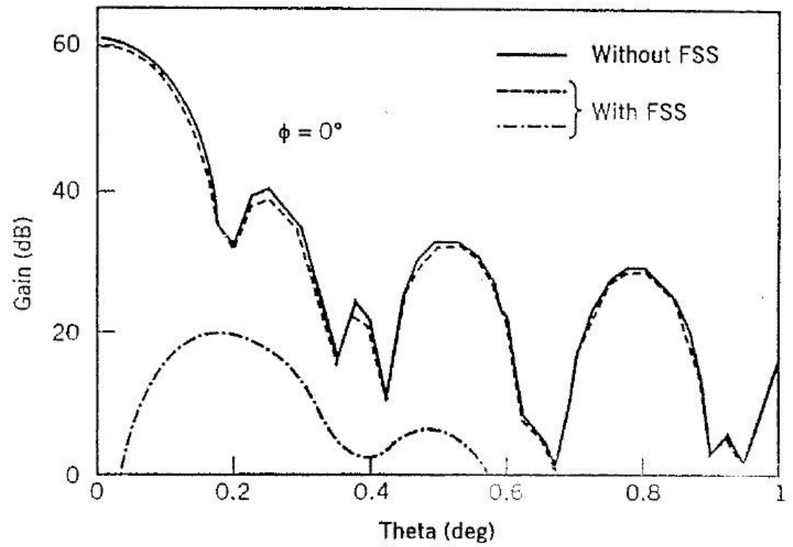


FIGURE 4.26(f) Far-field pattern of the HGA/FSS at 34.5 GHz.

from the subreflector rim. But, in the cases considered here, including this edge, diffracted fields only cause a 0.1-dB difference in the peak directivity. The computed peak directivity also agrees well with the PO-PO's results.

## 4.4 CONCLUSIONS

In this chapter a variety of multiband FSS designs are demonstrated with the superior gridded square-loop, double-ring, and double-square-loop patch elements. These FSSs were all designed by using the accurate integral equation technique described in Chapter 2 and Wu et al. [4–6]. The characteristics of double-screen FSS with nonsimilar design can be accurately predicted by the efficient single-mode cascading technique described in Chapter 3. The effects of the dielectric substrate and superstrate are also accurately evaluated by this technique. Good agreement between the mea-

TABLE 4.11. Cassini HGA / FSS Directivity Summary

| Frequency (GHz) | Directivity (dB) | FSS Insertion Loss (dB) |
|---|---|---|
| 2.3 | 37.94 | 0.72 |
| 7.2 | 47.61 | 0.41 |
| 8.4 | 48.95 | 0.16 |
| 13.8 | 53.5 | 0.2 |
| 32 | 60.57 | 0.68 |
| 34.5 | 61.22 | 1.09 |

sured and computed results verifies the various design approaches described in this chapter. Most important, they have been applied to advanced (low mass, volume, and cost) multiband reflector antenna systems for ground stations and spaceborne platforms.

## REFERENCES


1. G. H. Schennum, Frequency-selective surfaces for multiple frequency antennas. *Microwave J.* **16**, 55–57 (1973).
2. V. D. Agrawal and W. A. Imbriale, Design of a dichroic Cassegrain subreflector. *IEEE Trans. Antennas Propag.* AP-27(4), 466–473 (1979).
3. T. K. Wu and W. P. Shillue, Dichroic design for orbiting VLBI earth station antenna. *IEE Proc. MAP* **141**(3), 181–184 (1994).
4. T. K. Wu, M. Zimmerman, and S. W. Lee, Evaluation of frequency selective reflector antenna system. *Microwave Opt. Tech. Lett.* 6(3), 175–179 (1993).
5. J. Huang, T. K. Wu, and S. W. Lee, Tri-band FSS with circular ring elements. *IEEE Trans. Antennas Propag.* **AP-42**(2), 166–175 (1994).
6. T. K. Wu and S. W. Lee, Multi-band FSS with multi-ring patch elements. *IEEE Trans. Antennas Propag.* **AP-42**(11), 1484–1490 (1994).
7. T. K. Wu, Double-square-loop FSS for multiplexing four (S/X/Ku/Ka) bands. *Int. IEEE Antennas Propag. Symp. Dig.* London, Ontario, Canada, 1991, pp. 1885–1888 (1991).
8. T. K. Wu, Single screen triband FSS with double-square-loop elements. *Microwave Opt. Tech. Lett.* 5(2), 56–59 (1992).
9. P. Callagahan, E. Parker, and R. Langley, Influence of supporting dielectric layers on the transmission properties of frequency selective surfaces. *IEE Proc., Part H: Microwaves, Antennas Propag.* 138(5), 448–454 (1991).
10. C. K. Lee and R. Langley, Equivalent circuit models for frequency selective surfaces at oblique angle of incidence. *IEE Proc., Part H: Microwaves, Antennas Propag.* 132(6), 395–398 (1985).
11. E. Parker, R. Langley, R. Cahil, and J. Vardaxoglou, Frequency selective surface. *IEE Conf. Pub.* **219**, 459–463 (1983).
12. R. J. Langley and E. A. Parker, Double-square frequency-selective surfaces and their equivalent circuit. *Electron. Lett.* 19(17), 675 (1983).
13. C K. Lee and R. Langley, Equivalent circuit models for frequency selective surfaces at oblique angle of incidence. *IEE Proc., Part H: Microwaves, Antennas Propag.* (6), 395–398 (1985).
14. E. Parker, S. Hamdy, and R. Langley, Arrays of concentric rings as frequency selective surfaces. *Electron. Lett.* 17(2), 880 (1981).
15. E. A. Parker and J. C. Vardaxoglou, Plane-wave illumination of concentric-ring frequency-selective surfaces. *IEE Proc., Part H: Microwaves, Antennas Propag.* **132**, 176 (1985).





16. E. A. Parker and J. C. Vardaxoglou, Influence of single and multiple-layer dielectric substrates on the band spacings available from a concentric ring frequency-selective surface. *Int. J. Electron.* **61**, 291–297 (1986).
17. T. K. Wu, K. Woo, and S. W. Lee, Multi-ring element FSS for multi-band applications. *Int. IEEE Antennas Propag. Symp. Dig.*, Chicago, 1992, Vol. 4, pp. 1775–1778 (1992).
18. D. Bresciani and S. Contu, Scattering analysis of dichroic subreflectors. *Electromagnetics* 5(4), 375–407 (1985).